Research Article

Adaptive Fuzzy Control for Attitude Stabilization of Spacecraft with Deployable Composite Laminated Solar Array

Wei Zhang,[1] **Weibing Zhu** ⓘ**,**[1] **Shijie Zhang,**[2] **and Xiangtian Zhao**[2]

[1]*College of Aerospace and Civil Engineering, Harbin Engineering University, Harbin 150001, China*
[2]*School of Astronautics, Harbin Institute of Technology, Harbin 150001, China*

Correspondence should be addressed to Weibing Zhu; zhuweibing@hrbeu.edu.cn

Modern spacecraft are often equipped with large-scale, complex, and lightweight solar arrays whose deployment involves a highly dynamic movement. This paper proposed a novel adaptive proportional-derivative typed fuzzy logic control scheme for the attitude stabilization of a flexible spacecraft during the deployment of a composite laminated solar array. First, a constrained rigid-flexible coupling spacecraft model consisting of a rigid main body and a flexible solar array was proposed. The solar array, which is composed of composite laminated shells, was described by the absolute nodal coordinate formulation. Then, the detailed derivation of the adaptive fuzzy PD controller for attitude stabilization of the spacecraft was discussed. In addition, the spacecraft dynamic model which integrated the adaptive fuzzy PD controller was derived as a set of differential-algebraic equations. Several simulations were developed to investigate the solar array deployment dynamics and to verify the effectiveness of the proposed adaptive fuzzy PD controller. The results suggested that the proposed dynamic model is able to exactly describe the deployment dynamics of the composite laminated solar array. The solar array deployment causes obvious translational and rotational motions of the spacecraft. The proposed adaptive fuzzy PD control scheme has better performance in terms of the control precision and time response in stabilizing spacecraft during the deployment of the composite laminated solar array, comparing with that of the conventional PD controller.

1. Introduction

Modern spacecraft often employ large, complex, and lightweight solar arrays to achieve multiple functionalities and to provide sufficient power supply during flight [1]. The solar array deployment is a highly dynamic movement that may affect the spacecraft's motion [2–4]. In particular, when the locking operation is performed, the induced impulsive forces and moments may cause strong vibrations in large-scale and flexible solar panels. Consequently, it will severely affect spacecraft's motions, even leading to a disaster for a space mission. Therefore, an effective control scheme should be carried out to stabilize the spacecraft's motions during the deployment of solar arrays.

The first challenge is how to exactly describe the deployment dynamics of the solar array and evaluate its influence on the spacecraft main body. The spacecraft system is a typical constrained rigid-flexible coupling multibody system. In addition, these solar arrays are commonly composed of laminated shells involving fiber-reinforced composite materials, due to its high reliability, superior mechanical properties, high stiffness-to-weight ratio, and low fabrication cost [5–7]. The deployment of the composite laminated solar array exhibits a strong nonlinearity coupling between the large-rotation and large-deformation motions. Thus, an accurate dynamic model, which can well capture nonlinear characteristics (mainly including the material and geometric nonlinearity) of the solar array, plays a crucial role for the control scheme. Over the past few decades, several scholars have investigated the dynamics of the flexible multibody system involving the composite laminated plate/shell structures. Neto et al. [8] described the elastic deformations of a composite laminated plate undergoing large rigid body rotations by using the floating frame of the reference formulation (FFRF). Neto et al. [9] and Ambrósio et al. [10]

adopted the FFRF to study the deployment of a synthetic aperture radar antenna comprising composite laminated plates. The FFRF is a widely used method describing flexible multibody systems in the field of aerospace. However, mode reduction methods cannot be applied when the flexible multibody system experiences large deformations [11]. Additionally, the incremental finite element formulation and the large-rotation vector formulation are also used to describe the flexible multibody systems. These two formulations are capable of describing the large deformations of structures. However, the incremental finite element formulation cannot obtain the exact models of rigid motions when nonisoparametric elements are involved [12], and the large-rotation vector formulation will lead to singularity and unrealistic shear forces problems due to the redundancy [12]. The absolute nodal coordinate formulation (ANCF), originally developed by Shabana [13], utilizes global position vector gradients to model the rotation and deformation fields of the element, which can well describe the flexible body with large deformation in multibody applications. Also, it can avoid the coordinate redundancy problem [12] and singularities emerging from the parameterization of rotations [14] and can also induce a constant mass matrix. At present, several scholars started to show interest in studying the deployment dynamics of flexible multibody systems using ANCF. Li et al. [15] and Li et al. [16] investigated the deployment dynamics of a flexible solar array. The solar array was formulated with the planar deformable ANCF beam element. The planar deformable beam element is not enough when the solar array is a plate-formed structure in which the transverse shearing and the in-plane shearing exert nonnegligible influences on the dynamic response of the spacecraft. Liu et al. [17] adopted the ANCF to study the deployment dynamics of a flexible satellite antenna system comprising composite laminated plates. However, some convergence problems will emerge when the plate element is used to formulate very thin and stiff plates because of the plane stress assumption. Therefore, the deployment dynamics of composite laminated solar arrays still require further improved.

In the past few decades, spacecraft attitude control has gained huge attention. The conventional Proportional-Integration-Derivative (PID) or Proportional-Derivative (PD) control is the most popular industrial control method for simple structures due to its simplicity, reliability, and low-cost implementation [18–23]. The conventional PID/PD control has been widely applied to spacecraft attitude control systems and showed its feasibility and reliability in practical applications/implications [24, 25]. When designing a PD controller, the determination of design parameters is crucial. However, these design parameters cannot be accurately determined in most systems. In addition, the conventional PID/PD controller can accommodate disturbances to a certain extent, where the performance tends to be degraded under circumstances of significant disturbing sources [26]. Therefore, it is difficult for the conventional PID/PD controllers to achieve satisfactory performances with increasing functional requirements of spacecraft [20]. In recent years, the intelligent control scheme, which has evolved from the conventional control laws, has drawn more and more attention and performed better under the uncertainties

condition due to its high degree autonomy [27–33]. The fuzzy logic approach is one of the most widely used methods to observe the uncertainties in complex nonlinear systems [34–40]. Moreover, researchers have revealed that combining PID/PD with fuzzy logic techniques would result in a much better control scheme. Wang and Kwok [41] designed an intelligent control system by using the fuzzy set theory and the PID principle. Boubertakh et al. [42] proposed auto-tuning fuzzy PD and PI controllers using the reinforcement learning algorithm for single-input single-output and two-input two-output systems. Duan et al. [43] revealed a property of inherent saturation in the fuzzy PID controller. Further, Kumar and Kumar [44], Wang et al. [45], and Gomaa Haroun et al. [46, 47] have introduced new methods to improve the performance of the fuzzy PID/PD controller. These above studies confirmed that the adaptive fuzzy PID/PD control scheme could effectively improve the control performance and efficiency. The adaptive fuzzy PID/PD control scheme has also been gradually applied to the spacecraft attitude control. Kosari et al. [48] proposed a fuzzy PID control scheme based on genetic algorithms during a docking manoeuvre of two spacecraft. Calvo et al. [49] compared the adaptive fuzzy logic PID controller with conventional PID controller for the attitude control of a nanosatellite. The results showed that the adaptive fuzzy PID controller was significantly more efficient than the conventional PID. Chen et al. [50] proposed an adaptive fuzzy PD + controller for the attitude manoeuvre of a rigid spacecraft. Chak et al. [51] discussed a new composite control scheme combining disturbance observer-based control and fuzzy PD control for flexible spacecraft attitude control in the presence of external and internal disturbances caused by flexible appendages. The results showed that the fuzzy PD controller can effectively manoeuvre the spacecraft to the nadir attitude reference trajectory in the presence of multiple disturbances. Najafizadeh et al. [52] designed a novel fuzzy PID controller for geostationary satellite attitude control, which achieved faster convergence rates and higher accuracy. Li et al. [4, 53] designed a fuzzy PD controller to compensate for the attitude change of the spacecraft caused by the deployment of solar arrays. Although the above mentioned studies have investigated the adaptive fuzzy PID/PD control scheme for attitude control of the spacecraft, there are very few researches on eliminating the attitude and position drift caused by the deployment of solar arrays. In addition, modern spacecraft often employ large, complex, and lightweight solar arrays which are commonly composed of laminated plates with fiber-reinforced composite materials. The flexibility of solar arrays, nonlinearity of composite material, and other external disturbances may cause unpredictable rotational and translational motion of the spacecraft during the deployment of solar arrays. Therefore, a robust enough control scheme is required to overcome the model uncertainty and nonlinearity, structural vibrations of the flexible solar arrays, and the other disturbances in the environment. To the authors' best knowledge, studies related to this topic are not sufficient.

Our work aims to develop a constrained rigid-flexible coupling dynamic model of a spacecraft system equipped

with laminated solar arrays, involving fiber-reinforced composite materials, and further to propose an effective control scheme to stabilize the spacecraft main body during the deployment of the solar arrays. The key points of our work can be briefly described as follows. (1) A constrained rigid-flexible coupling spacecraft dynamic model was developed based on ANCF. The dynamic model can accurately describe the deployment dynamics of the composite laminated solar array undergoing large-rotation and large-deformation motions. (2) An adaptive fuzzy PD control scheme, which can be easily integrated into the spacecraft dynamic model, was proposed. (3) The computation strategies used to solve equations of motion of the spacecraft were provided in detail. The remainder of this paper is organized as follows. Section 2 first depicts the structure of the spacecraft system. The rigid-flexible coupling spacecraft dynamic model was then derived in Section 3. After that, Section 4 reveals the adaptive fuzzy PD control scheme. Section 5 gives equations of motion with the constrained rigid-flexible coupling dynamics and their solution strategies. After that, numerical simulations were conducted and analysed in Section 6. Finally, the whole work was summarised in Section 7.

2. Structure of Spacecraft System

This section illustrates the structure of a spacecraft with a deployable composite laminated solar array. As shown in Figure 1, the spacecraft system is simplified to a main body and a deployable solar array. The solar array mainly contains three types of critical devices, namely, the spring-damper mechanism (Figure 2(a)), the closed cable loop (CCL) mechanism (Figure 2(b)), and the latch mechanism (Figure 2(c)). These devices generate torque to realize the deployment of the solar array. The torque model is given in Figure 2(d). Three assumptions are made for the spacecraft system. (1) The main body and yoke are considered to be a completely free rigid unit. (2) The solar array is assembled with two flexible solar panels, connected by revolute joints. (3) The solar panel is assumed to be a perfect composite laminated shell; that is, there is no relative motion between any two layers of the composite laminated shell.

The spring-damper mechanism, which is located in the revolute joint, provides driving torque to deploy the folded solar array with the expression as

$$T_{\text{drive},k} = K_{\text{drive},k}\left(\theta_{\text{pre},k} - \theta_k\right) - C_k\frac{d\theta_k}{dt}, \qquad (1)$$

where $K_{\text{drive},k}$ is the torsion stiffness coefficient of the k-th spring-damper, C_k is the damping coefficient of the k-th spring-damper, and $\theta_{pre,k}$ and θ_k denote the preload angle and practical deployment angle of the solar panel, respectively.

The CCL mechanism comprises synchronous wheels fixed on the revolute joint and provides two passive control torques to synchronize the deployment angles of the solar panels [54]. The control torques can be simply modelled as [15]

$$\begin{cases} T_{\text{ccl},1} = K_{\text{ccl},1}\left(2\theta_1 - \theta_2\right), \\ T_{\text{ccl},2} = K_{\text{ccl},2}\left(2\theta_1 - \theta_2\right), \end{cases} \qquad (2)$$

where $T_{\text{ccl},1}$ and $T_{\text{ccl},2}$ are the equivalent synchronous torques and $K_{\text{ccl},1}$ and $K_{\text{ccl},2}$ are the equivalent torsional stiffness of the wheels. In addition, θ_1 and θ_2 are the deployment angles of the first and the second solar panel, respectively.

A typical latch mechanism is demonstrated in Figure 2(c). Body A is connected to the body B, and both of them can rotate around joint C. Cam E is fixed on body A, and pin F can move on cam E's surface during the deployment process. Pin F slides into groove D when the deployment angle reaches the preset lock angle, and, thus, body A and body B are latched at the expected position. The STEP and BISTOP functions are adopted to simulate this locking process. When the deployment angle θ_k increases from φ_1 to φ_2, the STEP function correspondingly increases from h_1 to h_2. Once the deployment angle θ_k reaches the collision point ($\varphi_3 \sim \varphi_4$), the BISTOP function begins to produce torques to push pin F toward the expected angle. These lock torques can be expressed as [15, 53]

$$T_{\text{lock},k} = \text{STEP}\left(\theta_k, \varphi_1, 0, \varphi_2, 1\right) \times \text{BISTOP}\left(\theta_k, \dot{\theta}_k, \varphi_3, \varphi_4, K_s, e, c, d\right), \qquad (3)$$

where

$$\text{STEP}\left(\theta_k, \varphi_1, h_1, \varphi_2, h_2\right) = \begin{cases} 0 & \text{if } \theta_k < \varphi_1, \\ h_1 + \left(h_2 - h_1\right)\left(\dfrac{\theta_k - \varphi_1}{\varphi_2 - \varphi_1}\right)^2\left(3 - 2\times\dfrac{\theta_k - \varphi_1}{\varphi_2 - \varphi_1}\right) & \text{if } \varphi_1 \le \theta_k < \varphi_2, \\ 1 & \text{if } \varphi_2 < \theta_k, \end{cases} \qquad (4)$$

$$\text{BISTOP}\left(\theta_k, \dot{\theta}_k, \varphi_3, \varphi_4, K_s, e, c, d\right) = \begin{cases} \text{Max}\left(K_s\left(\varphi_3 - \theta_i\right)^e - \dot{\theta}_i\text{STEP}\left(\theta_i, \varphi_3 - d, c, \varphi_3, 0\right), 0\right) & \text{if } \theta_k < \varphi_3, \\ \text{Min}\left(-K_s\left(\theta_k - \varphi_4\right)^e - \dot{\theta}_i\text{STEP}\left(\theta_i, \varphi_4, 0, \varphi_4 + d, c\right), 0\right) & \text{if } \theta_k > \varphi_4, \end{cases}$$
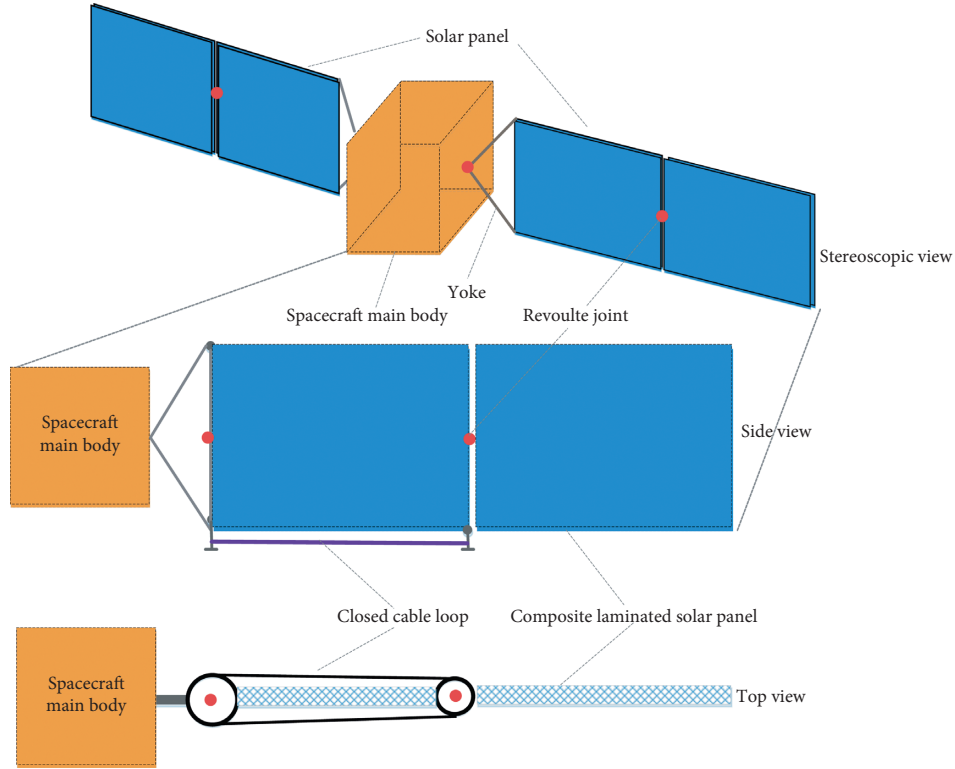
FIGURE 1: Scheme diagram of the spacecraft structure.

where $\dot{\theta}_k$ is the relative rotation velocity of the k-th solar panel. K_s and c are the equivalent stiffness and damping coefficients of the latch mechanism, respectively, d denotes the distance depth, and e is an exponent.

3. Formulation of Rigid-Flexible Coupling Spacecraft System

This subsection is divided into three parts to introduce the formulation of the spacecraft system, corresponding to the motion of the rigid main body, formulation of the composite laminated solar panel, and the motion of constraints. Without loss of generality, the spacecraft main body is regarded as a rigid body of arbitrary shape. As exhibited in Figure 3, an arbitrary point Q is attached to the rigid body. The global position vector of the point Q can be written as

$$r_Q = r + As', \tag{5}$$

where $r \in \mathbb{R}^{3 \times 1}$ is the global position vector of the origin of local coordinate frame x-y-z which is fixed on the rigid body. It should be noted that the local coordinate frame is selected with its origin at the center of mass of the body to simplify the form of the formulation. In equation (5), the local position of the point $s' = \begin{bmatrix} x & y & z \end{bmatrix}^{\mathrm{T}}$ is a constant vector because of the rigid body assumption, and A is the transformation matrix that defines the orientation of the local coordinate frame with respect to the global reference frame. Thus, the velocity of the point Q can be expressed as

$$\dot{r}_Q = \dot{r} + \dot{A}s' = \dot{r} + \tilde{\omega}As', \tag{6}$$

and the acceleration can be written as

$$\ddot{r}_Q = \ddot{r} + \ddot{A}s' = \ddot{r} + \tilde{\dot{\omega}}As' + \tilde{\omega}\tilde{\omega}As', \tag{7}$$

where ω is the angular velocity of the local coordinate frame with respect to the global coordinate frame. Without the singularity problem, the quaternion p is applied to describe the attitude of the spacecraft main body with the expression as

$$p = \left[\cos\frac{\theta}{2}, u\sin\frac{\theta}{2} \right]^{\mathrm{T}} = \left[\cos\frac{\theta}{2}, u_1\sin\frac{\theta}{2}, u_2\sin\frac{\theta}{2}, u_3\sin\frac{\theta}{2} \right]^{\mathrm{T}}, \tag{8}$$

where $u = \begin{bmatrix} u_1 & u_2 & u_3 \end{bmatrix}$ represents the Euler axis and θ is the angle of the rotation. And then, the generalized coordinate vector of the body can be defined with the quaternion as

$$q_b = \begin{bmatrix} r \\ p \end{bmatrix}. \tag{9}$$
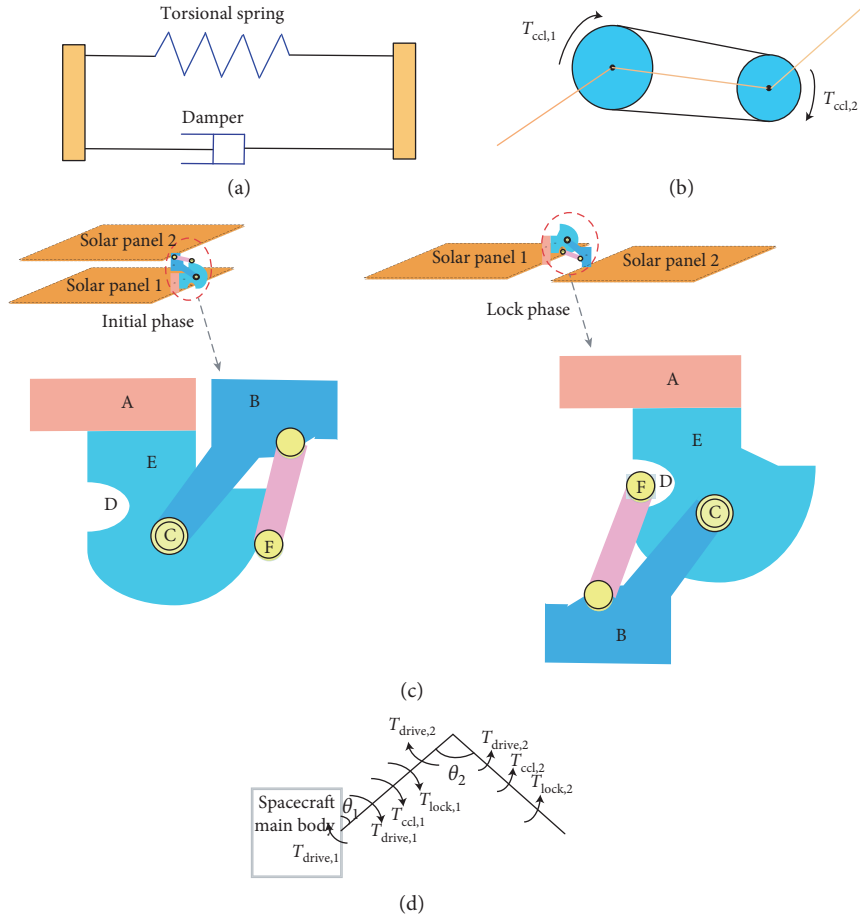
FIGURE 2: Representations of the solar array's mechanisms and torque models. (a) Spring-damper mechanism. (b) CCL mechanism. (c) Latch mechanism. (d) Torque model of the solar array.

The virtual work done by the inertial force can be expressed as [55]

$$\delta W_{ine}^b = -\delta r^T m \ddot{r} - \delta p^T \left(4G^T JG\ddot{p} - 8\dot{G}^T JG\dot{p} \right) = -\delta q_b^T \begin{bmatrix} m \\ & 4G^T JG \end{bmatrix} \ddot{q}_b + \delta q_b^T \begin{bmatrix} 0 \\ 8\dot{G}^T JG\dot{p} \end{bmatrix}, \qquad (10)$$

where m is the mass of the body, J is the constant inertia tensor which is defined as

$$J = \int_m \begin{bmatrix} y^2 + z^2 & -xy & -xz \\ -xy & x^2 + z^2 & -yz \\ -xy & -yz & x^2 + y^2 \end{bmatrix} dm, \qquad (11)$$

and G is the function of the quaternion p with the following expression:

$$G = \left[-u \sin \frac{\theta}{2}, -\tilde{u} \sin \frac{\theta}{2} + \cos \frac{\theta}{2} I \right]. \qquad (12)$$

The generalized mass matrix of the body can be defined as

$$M_b = \begin{bmatrix} m \\ & 4G^T JG \end{bmatrix}. \qquad (13)$$

If an external force F_b acts on the body at point Q, the virtual work of the body done by the external force can be obtained by

$$\delta W_{ext}^b = \delta r^T F_b + \delta p^T \left(2G^T n \right) = \delta q_b^T \begin{bmatrix} F_b \\ 2G^T n \end{bmatrix}, \qquad (14)$$

where n is the torque generated by the external forces acting at a distance from the origin of the local coordinate frame. The detailed derivation of the virtual work done by the inertial force and the external force can be found in Appendix A. Using equations (10) and (14), we can define the generalized external force as
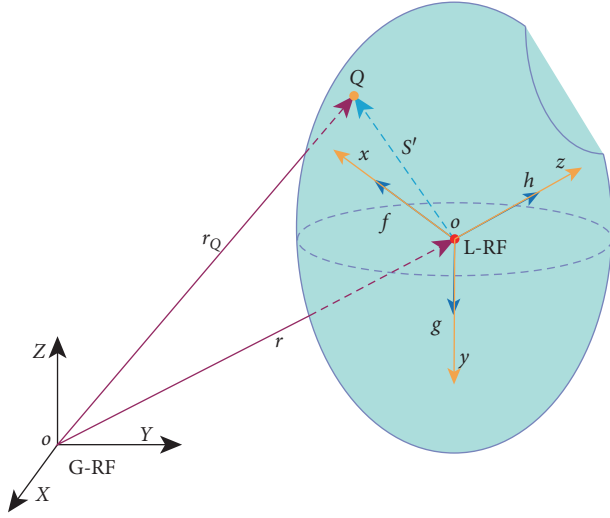
Figure 3: Kinematic description of the rigid body.

$$Q_{ext}^b = \begin{bmatrix} F_b \\ 2G^Tn + 8\dot{G}^T J\dot{G}p \end{bmatrix}. \quad (15)$$

The deformable ANCF laminated shell element, originally proposed by Yamashita et al. [56, 57], is employed to formulate the composite laminated solar panel. As shown in Figure 4, the global position vector of an arbitrary point P whose local coordinate is $(x\; y\; z)$ in shell element can be expressed as

$$r_P = r_m + zr_n = S_m q_m + z S_m q_n = \begin{bmatrix} S_m & z S_m \end{bmatrix} \begin{bmatrix} q_m \\ q_n \end{bmatrix}, \quad (16)$$

where r_m is the global position vector of the vertical projection point of P on the middle surface of the element and r_n is the transverse gradient vector that describes the orientation and deformation of the infinitesimal volume in the element. The global position vector of four corner nodes in the middle surface of the element and their transverse displacement gradient can be, respectively, written as

$$\begin{cases} q_m = \begin{bmatrix} r_1^T & r_2^T & r_3^T & r_4^T \end{bmatrix}^T, \\ q_n = \begin{bmatrix} \left(\frac{\partial r_1}{\partial z}\right)^T & \left(\frac{\partial r_2}{\partial z}\right)^T & \left(\frac{\partial r_3}{\partial z}\right)^T & \left(\frac{\partial r_4}{\partial z}\right)^T \end{bmatrix}^T, \end{cases} \quad (17)$$

where $r_i \in \mathbb{R}^{3\times 1}$ $(i = 1, 2, 3, 4)$ is the global position vector of each node. In (16), S_m is the element shape function defined as [43]

$$S_m = \begin{bmatrix} S_1 I & S_2 I & S_3 I & S_4 I \end{bmatrix}, \quad (18)$$

where $I \in \mathbb{R}^{3\times 3}$ is the identity matrix and S_i $(i = 1, 2, 3, 4)$ are components of the shape function obtained by

$$\begin{cases} S_1 = \frac{1}{4}(1 - \xi)(1 - \eta), & S_2 = \frac{1}{4}(1 + \xi)(1 - \eta), \\ \\ S_3 = \frac{1}{4}(1 + \xi)(1 + \eta), & S_4 = \frac{1}{4}(1 - \xi)(1 + \eta), \end{cases} \quad (19)$$

where $\xi = 2x/l$ and $\eta = 2y/w$. l and w are lengths along the x and y axes, respectively. Then, equation (16) can be simplified as

$$r_P = S q_e \quad (20)$$

where

$$\begin{cases} \mathbf{S} = \begin{bmatrix} \mathbf{S}_m & z\mathbf{S}_m \end{bmatrix}, \\ \mathbf{q}_e = \begin{bmatrix} \mathbf{q}_m & \mathbf{q}_n \end{bmatrix}^T. \end{cases} \quad (21)$$

According to the kinematic description of the element, the Green-Lagrange strain tensor is defined as

$$\boldsymbol{\varepsilon} = \frac{1}{2}\left[\left(\frac{\partial r_P}{\partial x}\left(\frac{\partial X}{\partial x}\right)^{-1}\right)^T \left(\frac{\partial r_P}{\partial x}\left(\frac{\partial X}{\partial x}\right)^{-1}\right) - I \right], \quad (22)$$

where x and X denote the local and the global position vector of the material point at the reference configuration, respectively. The element locking may occur in the deformable ANCF shell element due to the use of low-order polynomials in the shape function. The element lock leads to slower convergence in numerical iterations and erroneous stiffer bending behaviour. Thus, the assumed natural strain in [58, 59] and the enhanced assumed strain in [60, 61] are adopted to systematically alleviate the element locking. The modified strain vector can be defined as

$$\hat{\varepsilon} = \varepsilon + \varepsilon^{EAS}, \quad (23)$$

where ε^{EAS} denotes the enhanced assumed strain vector which is referred in literature [56]. All layers with different fiber angles are assumed to be bonded together to produce the desired material properties. Therefore, the virtual work done by elastic forces of the laminated shell element with n layers can be expressed as [57]

$$\delta W_{ela}^e = -\delta q_e^T \sum_{i=1}^{n} \int_{V^i} \left(\frac{\partial \varepsilon^i}{\partial q_e}\right)^T \frac{\partial W^i(\hat{\varepsilon}^i)}{\partial \varepsilon^i} dV^i, \quad (24)$$

where V^i is the element volume of the i-th layer at the reference configuration and W^i is an elastic energy density function that is described in Appendix B. Correspondingly, the generalized elastic forces of the element can then be written as

$$Q_{ela} = \sum_{i=1}^{n} \int_{V^i} \left(\frac{\partial \varepsilon^i}{\partial q_e}\right)^T \frac{\partial W^i(\hat{\varepsilon}^i)}{\partial \varepsilon^i} dV^i. \quad (25)$$
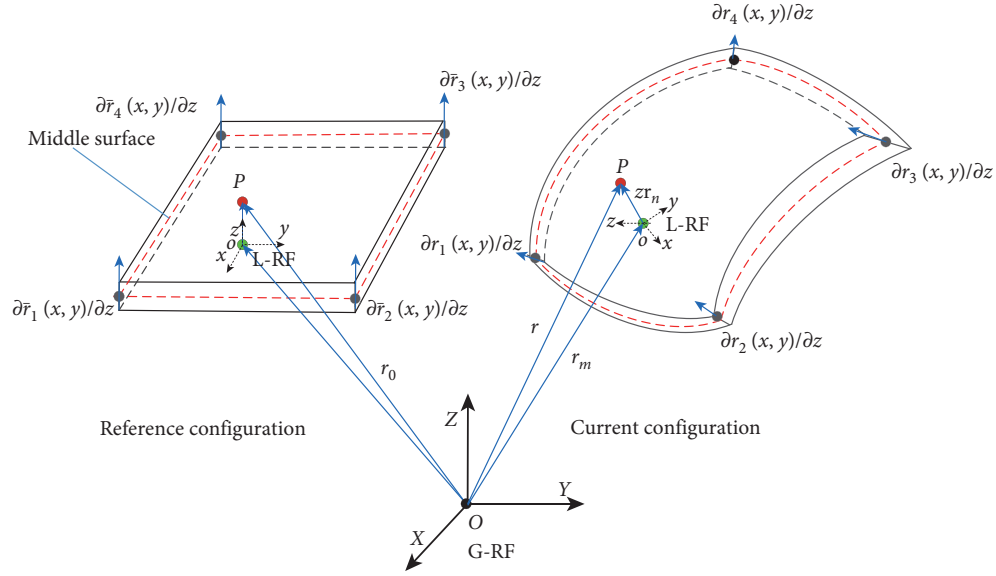
FIGURE 4: Kinematic description of the deformable ANCF shell element.

The shape function of the element is not time-dependent, and, then, the element's kinetic energy can be defined as

$$T = \frac{1}{2} \sum_{k=1}^{n} \int_{V^i} \rho^i \left(\dot{r}_P \right)^{\mathrm{T}} \dot{r}_P \mathrm{d}V^i = \frac{1}{2} \dot{q}_e^{\mathrm{T}} \sum_{k=1}^{n} \int_{V^i} \rho^i S^{\mathrm{T}} S \mathrm{d}V^i \dot{q}_e, \tag{26}$$

where ρ^i is the material density of the i-th layer at the reference configuration. Then, the constant mass matrix can be obtained by

$$M_e = \sum_{k=1}^{n} \int_{V^i} \rho^i S^{\mathrm{T}} S \mathrm{d}V^i. \tag{27}$$

Hence, the virtual work done by the inertia forces on the element can be expressed as

$$\delta W_{ine}^e = -\delta q_e^{\mathrm{T}} \left(M_e \ddot{q}_e \right). \tag{28}$$

Denoting by F_e the external force acts on the element, we can write the following virtual work:

$$\delta W_{ext}^e = \delta r_P^{\mathrm{T}} F_e = \delta q_e^{\mathrm{T}} \left(S^{\mathrm{T}} F_e \right). \tag{29}$$

The generalized external force vector of the element can be obtained by

$$Q_{ext}^e = S^{\mathrm{T}} F_e. \tag{30}$$

It should be noted that the driving torques of the spring-dampers in equation (1), the synchronization torques of the CCL mechanisms in equation (2), and the lock torques of the latch mechanisms in equation (3) are regarded as the external forces of the shell. These torques are then integrated into the generalized external force vector. With the assumption that the structural damping exists in the shell, the virtual work done by the damping forces can be defined as

$$\delta W_{dam}^e = -\delta q_e^{\mathrm{T}} D \dot{q}_e, \tag{31}$$
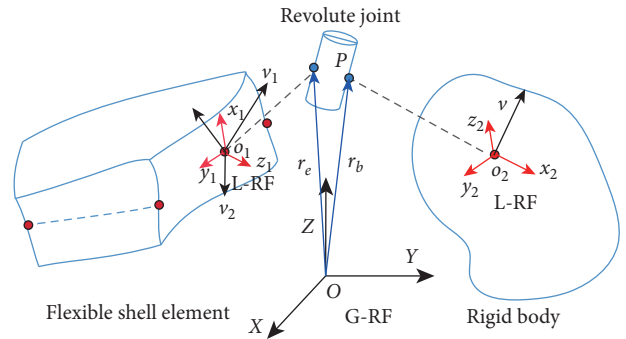
FIGURE 5: Kinematic description of the revolute joint.

where $D = \zeta M_e$ is the damping matrix and ζ is the damping coefficient.

The rigid main body and flexible solar panels are linked by revolute joints, which can be represented by a constraint equation. As depicted in Figure 5, a shell element is connected to a rigid body at point P by a revolute joint, and the constraint equation can be defined as [58, 59]

$$\Phi \left(q_e, q_b, t \right) = \begin{bmatrix} r_e - r_b \\ v_1^{\mathrm{T}} v \\ v_2^{\mathrm{T}} v \end{bmatrix} = 0, \tag{32}$$

where q_e and q_b are the generalized coordinate vectors of point P defined on element and rigid body, respectively, r_e and r_b are the global position vectors of point P defined on the element and rigid body, respectively, and v_i $(i = 1, 2)$ and v are vectors defined along the joint axis on shell element and rigid body, respectively. We can then obtain the virtual work done by constraint forces [62]:

$$\delta W_{\text{con}} = \lambda^{\text{T}} \delta \Phi = \lambda^{\text{T}} \frac{\partial \Phi}{\partial q_e} \delta q_e + \lambda^{\text{T}} \frac{\partial \Phi}{\partial q_b} \delta q_b = \delta q_e^{\text{T}} \left(\Phi_{q_e}^{\text{T}} \lambda \right) + \delta q_b^{\text{T}} \left(\Phi_{q_b}^{\text{T}} \lambda \right), \tag{33}$$

where λ is the Lagrange multipliers vector corresponding to the vector Φ. $\Phi_{q_e} = \partial \Phi / \partial q_e$ and $\Phi_{q_b} = \partial \Phi / \partial q_b$ are Jacobian matrices with expression as follows:

$$\begin{bmatrix} \dfrac{\partial \Phi}{\partial q_e} & \dfrac{\partial \Phi}{\partial q_b} \end{bmatrix} = \begin{bmatrix} \dfrac{\partial r_e}{\partial q_e} & -\dfrac{\partial r_b}{\partial q_b} \\ v^{\text{T}} \dfrac{\partial v_1}{\partial q_e} & v_1^{\text{T}} \dfrac{\partial v}{\partial q_b} \\ v^{\text{T}} \dfrac{\partial v_2}{\partial q_e} & v_2^{\text{T}} \dfrac{\partial v}{\partial q_b} \end{bmatrix}. \tag{34}$$

4. Adaptive Fuzzy PD Control Scheme

As discussed in the previous section, the deployment of solar arrays may cause attitude and position perturbations within spacecraft. We first observe the conventional PD control scheme in the elimination of position deviations and attitude stabilization during the deployment of solar arrays.

It is well known that reaction wheel actuators are commonly employed to provide control forces and torques, which can accommodate position deviations and finite rotations caused by the deployment of solar arrays. Assuming that $r_a(t) = \begin{bmatrix} r_{a,x} & r_{a,y} & r_{a,z} \end{bmatrix}$ and $r_d(t) = \begin{bmatrix} r_{d,x} & r_{d,y} & r_{d,z} \end{bmatrix}$ are the actual and the desired global position coordinate vectors of the main body, respectively, and $\dot{r}_a = \begin{bmatrix} \dot{r}_{a,x} & \dot{r}_{a,y} & \dot{r}_{a,z} \end{bmatrix}$ and $\dot{r}_d = \begin{bmatrix} \dot{r}_{d,x} & \dot{r}_{d,y} & \dot{r}_{d,z} \end{bmatrix}$ are the actual and desired velocity vectors of the main body, respectively, a PD controller for eliminating position deviations is presented as

$$\tau^f(t) = P^f e_p(t) + D^f \dot{e}_p(t), \tag{35}$$

where

$$P^f = \begin{bmatrix} K_{P,x}^f & 0 & 0 \\ 0 & K_{P,y}^f & 0 \\ 0 & 0 & K_{P,z}^f \end{bmatrix},$$

$$D^f = \begin{bmatrix} K_{D,x}^f & 0 & 0 \\ 0 & K_{D,y}^f & 0 \\ 0 & 0 & K_{D,z}^f \end{bmatrix},$$

$$e_p(t) = \begin{bmatrix} r_{d,x} - r_{a,x} \\ r_{d,y} - r_{a,y} \\ r_{d,z} - r_{a,z} \end{bmatrix},$$

$$\dot{e}_p(t) = \begin{bmatrix} \dot{r}_{d,x} - \dot{r}_{a,x} \\ \dot{r}_{d,y} - \dot{r}_{a,y} \\ \dot{r}_{d,z} - \dot{r}_{a,z} \end{bmatrix}, \tag{36}$$

in which $K_{P,i}^f (i = x, y, z)$ and $K_{D,i}^f (i = x, y, z)$ are the proportional and differential gains of the PD controller, respectively. Then, the virtual work done by these control forces can be expressed as

$$\delta W_f = \delta r^T \tau^f. \tag{37}$$

According to Euler's theorem of finite rotations of the rigid body, an arbitrary finite rotation of a rigid body over a fixed point can always be represented by the Euler axis and the angle of rotation [63]. In view of the attitude stabilization, we exploit three quaternions, including error quaternion p_e, actual quaternion p_a, and desired quaternion p_d, to describe the attitude deviation of the main body. The mathematical relationships of these quaternions are

$$p_e = (p_a)^{-1} p_d. \tag{38}$$

Now, three equivalent error angles $\begin{bmatrix} \theta_x & \theta_y & \theta_z \end{bmatrix}$ are defined using the error quaternion:

$$\begin{cases} \theta_x = p_e(2) p_e(1), \\ \theta_y = p_e(3) p_e(1), \\ \theta_z = p_e(4) p_e(1), \end{cases} \tag{39}$$

where $p_e(i), (i = 1, 2, 3, 4)$ are four components of the error quaternion p_e. Denoting the actual and the desire angular velocity vectors by $\omega_a = \begin{bmatrix} w_{a,x} & w_{a,y} & w_{a,z} \end{bmatrix}$ and $\omega_d = \begin{bmatrix} w_{d,x} & w_{d,y} & w_{d,z} \end{bmatrix}$, respectively, we can present the PD controller for attitude stabilization as

$$\tau^t(t) = P^t e_a(t) + D^t \dot{e}_a(t), \tag{40}$$

where

$$\mathbf{P}^t = \begin{bmatrix} K_{P,x}^t & 0 & 0 \\ 0 & K_{P,y}^t & 0 \\ 0 & 0 & K_{P,z}^t \end{bmatrix},$$

$$\mathbf{D}^t = \begin{bmatrix} K_{D,x}^t & 0 & 0 \\ 0 & K_{D,y}^t & 0 \\ 0 & 0 & K_{D,z}^t \end{bmatrix},$$

$$\mathbf{e}_a(t) = \begin{bmatrix} \alpha \\ \beta \\ \gamma \end{bmatrix},$$

$$\dot{\mathbf{e}}_a(t) = \begin{bmatrix} w_{d,x} - w_{a,x} \\ w_{d,y} - w_{a,y} \\ w_{d,z} - w_{a,z} \end{bmatrix}, \tag{41}$$

in which $K_{P,i}^t (i = x, y, z)$ and $K_{D,i}^t (i = x, y, z)$ are the proportional and differential gains of the PD controller, respectively. Thus, the virtual work done by these control torques can be obtained by

$$\delta W_t = \delta p^T \tau^t. \tag{42}$$

It is a challenging task to determine proper PD parameters when considering the flexibility of solar arrays, nonlinearity of the composite material, and other uncertainties. As a result, an adaptive fuzzy PD control scheme was proposed. The block diagram of the proposed control scheme is depicted in Figure 6. The adaptive fuzzy PD controller primarily consists of two parts: one is a fuzzy logic system and the other is a PD controller. In the
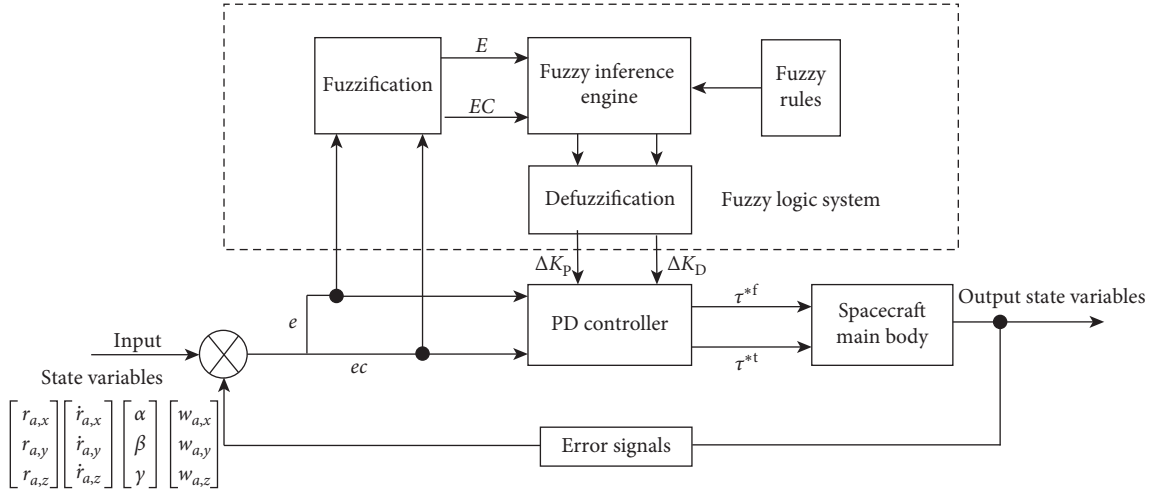
FIGURE 6: Schematic of the adaptive fuzzy PD control scheme.

control loop, the control gains are modified online using the fuzzy rules and sent to the PD controller. Firstly, error signals are computed according to the state variables of the spacecraft and the desired variables. The symbol e in the diagram includes actual position errors $r_d - r_a$ and attitude angle errors $\begin{bmatrix} \theta_x & \theta_y & \theta_z \end{bmatrix}$ while the symbol ec represents velocity errors $\dot{r}_d - \dot{r}_a$ and angular velocity errors $\omega_d - \omega_a$. These error signals are fuzzified by using membership functions and sent to the fuzzy inference engine. After that, the fuzzy inference engine performs the fuzzy reasoning on the basis of fuzzy rules to obtain the fuzzy proportional and differential gains. Finally, the PD controller updates its feedback gains in real time according to these fuzzy gains. The control forces and torques generated from the PD controller act on the spacecraft main body. Control actuators remain active until those error signals reach zero. The fuzzy logic system mainly includes four components, namely, fuzzification, fuzzy rules, fuzzy inference engine, and defuzzification. Fuzzification maps the input state errors (e and ec) into two fuzzy variables (E and EC) that are defined with three fuzzy sets where the associated linguistic terms are negative (N), zero (Z), and positive (P) by using membership functions. The fuzzy IF-THEN rules are adopted to relate these fuzzy sets to output fuzzy gains with the Mamdani-type fuzzy inference [53]. Defuzzification converts the output linguistic variables into precise numerical values. The center-of-gravity method is used to defuzzify the subset in the fuzzy logic system. Now, we give the expression of the control forces as follows:

$$\tau^{*f}(t) = P^{*f} e_p(t) + D^{*f} \dot{e}_p(t), \tag{43}$$

where

$$P^{*f} = \begin{bmatrix} K_{P,x}^f + \Delta K_{P,x}^f & 0 & 0 \\ 0 & K_{P,y}^f + \Delta K_{P,y}^f & 0 \\ 0 & 0 & K_{P,z}^f + \Delta K_{P,z}^f \end{bmatrix},$$

$$D^{*f} = \begin{bmatrix} K_{D,x}^f + \Delta K_{D,x}^f & 0 & 0 \\ 0 & K_{D,y}^f + \Delta K_{D,y}^f & 0 \\ 0 & 0 & K_{D,z}^f + \Delta K_{D,z}^f \end{bmatrix}, \tag{44}$$

in which $\Delta K_{P,i}^f$ and $\Delta K_{D,i}^f$ ($i = x, y, z$) are the fuzzy increments of the proportional and differential gains, respectively. The expression of the control forces can be written as

$$\tau^{*t}(t) = P^{*t} e_p(t) + D^{*t} \dot{e}_p(t), \tag{45}$$

where

$$P^{*t} = \begin{bmatrix} K_{P,x}^t + \Delta K_{P,x}^t & 0 & 0 \\ 0 & K_{P,y}^t + \Delta K_{P,y}^t & 0 \\ 0 & 0 & K_{P,z}^t + \Delta K_{P,z}^t \end{bmatrix},$$

$$D^{*t} = \begin{bmatrix} K_{D,x}^t + \Delta K_{D,x}^t & 0 & 0 \\ 0 & K_{D,y}^t + \Delta K_{D,y}^t & 0 \\ 0 & 0 & K_{D,z}^t + \Delta K_{D,z}^t \end{bmatrix}, \tag{46}$$

in which $\Delta K_{P,i}^t$ and $\Delta K_{D,i}^t$ ($i = x, y, z$) are the fuzzy increments of the proportional and differential gains, respectively. The total virtual work done by these forces and torques can be expressed as

$$\delta W_{fuz}^b = \delta W_f^* + \delta W_t^* = \delta r^{\mathrm{T}} \tau^{*f} + \delta p^{\mathrm{T}} \tau^{*t} = \delta q_b^{\mathrm{T}} \begin{bmatrix} \tau^{*f} \\ \tau^{*t} \end{bmatrix}, \tag{47}$$

and then the generalized control force can be defined as

$$Q_{\mathrm{fuz}}^b = \begin{bmatrix} \tau^{*f} \\ \tau^{*t} \end{bmatrix}. \tag{48}$$

5. Equations of Motion and Solve Strategy

According to the principle of virtual work, the variation equations of the whole rigid-flexible coupling spacecraft system can be written as

$$\left(\delta W_{\mathrm{ine}}^b + \delta W_{\mathrm{ext}}^b\right) + \left(\delta W_{\mathrm{ine}}^e + \delta W_{\mathrm{ela}}^e + \delta W_{\mathrm{ext}}^e + \delta W_{\mathrm{dam}}^e\right) + \delta W_{\mathrm{con}} = 0. \tag{49}$$

Substituting equations (10), (13)–(15), (24), (25), (28)–(31), (33), and (47) into (49) yields

$$
\left[-\delta q_b^{\mathrm{T}}(M_b\ddot{q}_b) + \delta q_b^{\mathrm{T}}Q_{\mathrm{ext}}^b + \delta q_b^{\mathrm{T}}Q_{\mathrm{fuz}}^b\right] + \delta q_e^{\mathrm{T}}\left(\Phi_{q_e}^{\mathrm{T}}\lambda\right) + \delta q_b^{\mathrm{T}}\left(\Phi_{q_b}^{\mathrm{T}}\lambda\right)
$$
$$
+ \left[-\delta q_e^{\mathrm{T}}\left(M_e\ddot{q}_e\right) + \delta q_e^{\mathrm{T}}Q_{\mathrm{ela}}^e + \delta q_e^{\mathrm{T}}Q_{\mathrm{ext}}^e - \delta q_e^{\mathrm{T}}D\dot{q}_e\right] = 0. \tag{50}
$$

Using equation (32), we can obtain equations of motion of the spacecraft:

$$
\begin{cases} M\ddot{q} + \Phi_q^{\mathrm{T}}\lambda + Q(q) = F(q,\dot{q}), \\ \Phi(q,t) = 0, \end{cases} \tag{51}
$$

where

$$
M = \begin{bmatrix} M_b & 0 \\ 0 & M_e \end{bmatrix},
$$
$$
Q(q) = \begin{bmatrix} 0 \\ -Q_{\mathrm{ela}}^e \end{bmatrix},
$$
$$
F(q,\dot{q}) = \begin{bmatrix} Q_{\mathrm{ext}}^b + Q_{\mathrm{fuz}}^b \\ Q_{\mathrm{ext}}^e - D\dot{q}_e \end{bmatrix},
$$
$$
q = \begin{bmatrix} q_b \\ q_e \end{bmatrix}. \tag{52}
$$

The Newmark method is used to discretize equation (51) as

$$
\begin{cases} M\ddot{q}_{n+1} + \Phi_q^T\lambda_{n+1} + Q(q_{n+1}) = F(q_{n+1},\dot{q}_{n+1}), \\ \Phi(q_{n+1},t_{n+1}) = 0, \end{cases} \tag{53}
$$

where

$$
\begin{cases} q_{n+1} = q_n + h\dot{q}_n + \dfrac{h^2}{2}\left((1-2\beta)\ddot{q}_n + 2\beta\ddot{q}_{n+1}\right), \\ \dot{q}_{n+1} = \dot{q}_n + h\left((1-\gamma)\ddot{q}_n + \gamma\ddot{q}_{n+1}\right), \end{cases} \tag{54}
$$

where β and γ are parameters for determining iteration convergence and accuracy, respectively. The Newmark method are generally poor in solving the dynamics problems of the multibody system with high-frequency responses [64]. Additionally, spurious high-frequency responses may exist in the spacecraft system, mainly due to the flexibility of solar arrays. Thus, it is desirable for an algorithm with a controllable numerical dissipation which can well-preserve the low-frequency responses and damp the high-frequency responses. Negrut et al. [65] proposed an HHT-based algorithm for the index 3 differential-algebraic equations of multibody systems, known as HHT-I3. According to ANCF, it has been demonstrated that the HHT-I3 method's high-frequency responses can be filtered out while preserving accuracy [66]. According to the HHT-I3 method, the iterative form can be written as [67]

$$
\begin{bmatrix} \dfrac{\partial N_1}{\partial \ddot{q}_{n+1}} & \dfrac{\partial N_1}{\partial \lambda_{n+1}} \\[2mm] \dfrac{\partial N_2}{\partial \ddot{q}_{n+1}} & \dfrac{\partial N_2}{\partial \lambda_{n+1}} \end{bmatrix} \begin{bmatrix} \Delta\ddot{q}_{n+1} \\ \Delta\lambda_{n+1} \end{bmatrix} = \begin{bmatrix} N_1 \\ N_2 \end{bmatrix}, \tag{55}
$$

where

$$
\begin{cases} N_1 = \dfrac{1}{1+\eta}M\ddot{q}_{n+1} + \Phi_q^{\mathrm{T}}\lambda_{n+1} + Q(q_{n+1}) - F(q_{n+1},\dot{q}_{n+1}) - \dfrac{\eta}{1+\eta}\left[\Phi_q^{\mathrm{T}}\lambda_n + Q(q_n) - F(q_n,\dot{q}_n)\right], \\[3mm] N_2 = \dfrac{1}{\beta h^2}\Phi(q_{n+1},t_{n+1}), \\[3mm] \dfrac{\partial N_1}{\partial \lambda_{n+1}} = \Phi_q^{\mathrm{T}}, \\[3mm] \dfrac{\partial N_2}{\partial \lambda_{n+1}} = 0, \\[3mm] \dfrac{\partial N_1}{\partial \ddot{q}_{n+1}} = \dfrac{1}{1+\eta}M + \dfrac{\partial Q}{\partial q_{n+1}}\dfrac{\partial q_{n+1}}{\partial \ddot{q}_{n+1}} - \left(\dfrac{\partial F}{\partial q_{n+1}}\dfrac{\partial q_{n+1}}{\partial \ddot{q}_{n+1}} + \dfrac{\partial F}{\partial q_{n+1}}\dfrac{\partial \dot{q}_{n+1}}{\partial \ddot{q}_{n+1}}\right), \\[3mm] \qquad = \dfrac{1}{1+\eta}M + \left(\dfrac{\partial Q}{\partial q_{n+1}} - \dfrac{\partial F}{\partial q_{n+1}}\right)\beta h^2 - \dfrac{\partial F}{\partial q_{n+1}}h\gamma, \\[3mm] \dfrac{\partial N_2}{\partial \ddot{q}_{n+1}} = \dfrac{1}{\beta h^2}\dfrac{\partial N_2}{\partial q_{n+1}}\dfrac{\partial q_{n+1}}{\partial \ddot{q}_{n+1}} = \Phi_q, \end{cases} \tag{56}
$$

where $\beta = (1 - \eta)^2/4$ and $\gamma = 0.5 - \eta$, $\eta \in [-(1/3)\,0]$, and the parameter η is a numerical damping index. Converting equation (55) into the explicit format at iteration k yields

$$\left[\begin{array}{cc} \dfrac{1}{1+\eta}M + \left(\dfrac{\partial Q}{\partial q_{n+1}} - \dfrac{\partial F}{\partial q_{n+1}}\right)\beta h^2 - \dfrac{\partial F}{\partial q_{n+1}}h\gamma & \Phi_q^T \\ \Phi_q & 0 \end{array}\right]^{(k)} \left[\begin{array}{c} \Delta\ddot{q}_{n+1} \\ \Delta\lambda_{n+1} \end{array}\right]^{(k)} = \left[\begin{array}{c} N_1 \\ N_2 \end{array}\right]^{(k)}. \tag{57}$$

Thus, the iteration can be written as

$$\left[\begin{array}{c} \ddot{q}_{n+1} \\ \lambda_{n+1} \end{array}\right]^{(k+1)} = \left[\begin{array}{c} \ddot{q}_{n+1} \\ \lambda_{n+1} \end{array}\right]^{(k)} - \left[\begin{array}{c} \Delta\ddot{q}_{n+1} \\ \Delta\lambda_{n+1} \end{array}\right]^{(k)}, \tag{58}$$

where the initial step can be set as [67]

$$\begin{cases} \dot{q}_0 = q_0 = 0, \\ \ddot{q}_0 = M^{-1}F. \end{cases} \tag{59}$$

6. Results and Discussion

6.1. Model Parameters. The solar array deployment is divided into three phases, namely, the initial phase, the deployment phase, and the postlock phase (see Figure 7). During the initial phase, the solar panels are folded and set parallel to each other. Once the spacecraft is launched into its free-flying orbit, the solar panels are driven to deploy by the preloaded spring-damper mechanism, and the CCL mechanism ensures the synchronous deployment. When the solar panels are deployed on the same spatial plane, the lock torques provided by the latch mechanism begin to confine relative rotation of the panels. At this time and thereafter, the solar array deployment enters its postlock phase. The global coordinate system, which is the absolute reference for the spacecraft system's motions, is set up and its origin is at the center of mass of spacecraft main body. The geometrical dimensions of the vital components of the system are labeled in the figure.

Several simulations are conducted to confirm the effectiveness of the proposed control scheme. It is assumed that the geometrical dimensions and material properties of the main body as well as physical parameters of the solar array mechanisms keep identical in all simulations. Simulation parameters are listed in Table 1. The numerical simulations for the proposed adaptive fuzzy PD control scheme were performed under cosimulation of Visual Stuido 2017 and MATLAB R2017 software. In these numerical calculations, the adaptive fuzzy PD control algorithms are implemented by MATLAB/Simulink, and the numerical algorithms for solving the equations of the proposed rigid-flexible coupling dynamic model are implemented by C++ programs. Each flexible solar panel is divided into 120 elements.

6.2. Model Validation. In this subsection, two simulations are carried out to verify the proposed model. The first simulation presents a cantilevered shell subjected to a vertical force to reveal the mechanical properties of the deformable ANCF laminated shell element adopted in this paper. As shown in Figure 8, a rectangular cantilevered composite laminated shell with four layers (0/45/−45/0) is subjected to a force in the Z direction. The geometric size of the composite laminated shell is $5 \times 3 \times 0.008$ m. The material properties of these four layers are the same: Young's modulus $E_1 = 6.78 \times 10^8$ Pa, $E_2 = E_3 = 4.08 \times 10^8$ Pa, Shear modulus $G_{12} = G_{13} = 1.20 \times 10^8$ Pa, $G_{23} = 4.50 \times 10^8$ Pa, Poisson's ratio $\nu_{12} = \nu_{13} = \nu_{23} = 0.3$, and material density $\rho = 150$ kg/m^3. A vertical force in the Z direction is applied on point B which is located at the far right corner of the shell (viewed from the clamped boundary).

A contrast study is made between the deformable ANCF laminated shell and the laminated shell with finite membrane strains modelled by ABAQUS S4R elements. As shown in Figure 9, the displacement responses at point B are compared along the X (Figure 9(a)), Y (Figure 9(b)), and Z (Figure 9(c)) directions. The displacement curves obtained by the deformable ANCF laminated shell elements match well with those obtained by the ABAQUS S4R laminated shell element, which indicate that the deformable ANCF laminated shell element in this paper clearly describes a flexible body undergoing large deformations.

The spacecraft in this study is a typical rigid-flexible coupling system with a flexible solar array formulated with deformable ANCF composite laminated shell element. An identical rigid-flexible coupling model was achieved by using the cosimulation of ADAMS-ABAQUS. The rigid main body is modelled by ADAMS software, and the flexible solar panels are constructed of largely deformable ABAQUS S4R laminated shell element. Figure 10 shows the comparison results for the angular displacements of the two solar panels. As illustrated in Figures 10(a) and 10(b), the angular displacement curves obtained by the proposed model almost coincide with those obtained by ADAMS-ABAQUS software, suggesting that the proposed model is valid.

6.3. Dynamic Responses of Spacecraft System. This subsection presents the position and attitude responses of the main body during the deployment of the solar array. Figure 11 shows the solar panel deployment process. Figures 11(a) and 11(b) depict the angular displacements of solar panel 1 and solar panel 2, respectively. In the initial phase, the solar panels are folded, as well as setting parallel to each other, and their angular displacements are zero or near zero. After the solar array is released, the two solar panels are deployed through the torsional spring-damper mechanisms. The deployment angles are controlled by the CCL mechanism, with a proportionality coefficient of 0.5. The system is then locked by the latch mechanism at about the 18th second, when the lock torques are produced by the latch mechanism to prevent relative rotation of the two panels. In the postlock phase, there are some slight oscillations in the angular displacements of the panels. These oscillations are mainly caused by impact forces from the latch mechanisms. After that, the system maintains a relatively steady deployment

(a)

(b)
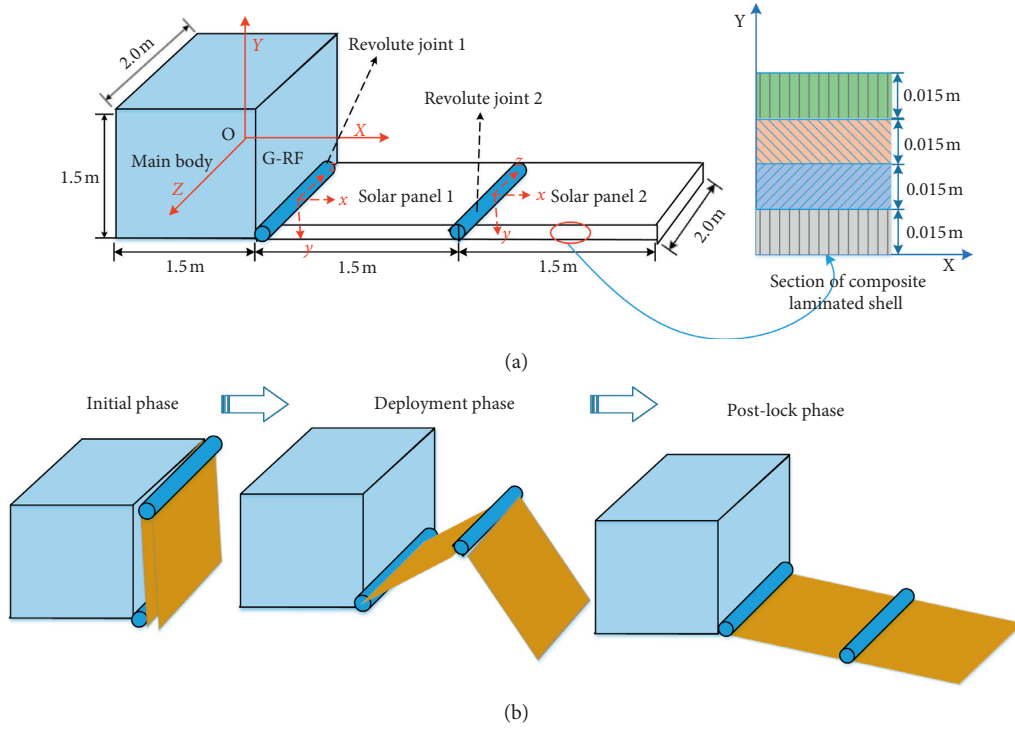
FIGURE 7: Deoployment process of the solar array.

TABLE 1: Physical parameters of the spacecraft system.

Parameter item	Parameter value
Size of the main body (m)	$1.5 \times 1.5 \times 2.0$
Material density of the main body (kg/m^3)	2400
Length of panels (m)	1.5
Width of panels (m)	2.0
Thickness of panels (m)	0.06
Material density of panels (kg/m^3)	100
Young's modulus of panels (Pa)	$E_1 = 6.78 \times 10^8$, $E_2 = E_3 = 4.08 \times 10^8$
Poisson's ratio of panels (-)	$v_{12} = v_{13} = v_{23} = 0.3$
Shear modulus of panels (Pa)	$G_{12} = G_{13} = 1.2 \times 10^8$, $G_{23} = 4.5 \times 10^8$
Layer number of panels (-)	4
Fiber angle relative to the Y direction (°)	0/90/90/0
Material thickness of panels (m)	0.015/0.015/0.015/0.015
Torsional stiffness of spring-damper 1 (N m/rad)	0.25
Torsional stiffness of spring-damper 2 (N m/rad)	0.085
Damping coefficient of spring-damper 1 (N/(m/s))	0.025
Damping coefficient of spring-damper 2 (N/(m/s))	0.015
Equivalent cable stiffness of CCL 1 (N m/rad)	60
Equivalent cable stiffness of CCL 2 (N m/rad)	15
Equivalent stiffness of latch 1 (N m/rad)	2.5×10^4
Equivalent stiffness of latch 2 (N m/rad)	1×10^4
Damping coefficient of latch 1 (N/(m/s))	2.5×10^3
Damping coefficient of latch 2 (N/(m/s))	1×10^3
Exponent of latch 1 and latch 2 (-)	1.5
Distance depth of latch 1 and latch 2 (°)	0.01
Time step (s)	0.001
Total time (s)	40

state in the plane with deployment angles of nearly 0.5 π for panel 1 and nearly π for panel 2.

The torque responses of three types of mechanisms mentioned in the previous section are critical for the whole spacecraft system. Figure 12 shows the torque responses of these mechanisms for solar array deployment. Figure 12(a) shows that the driving torques of the two spring-dampers reach the peak during the initial phase, and, then, both
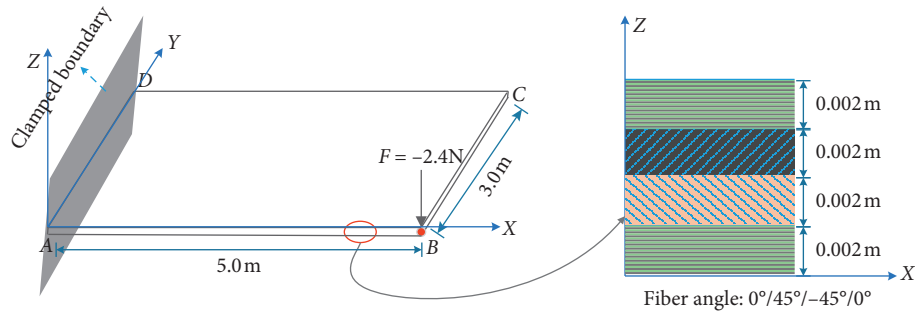
FIGURE 8: A cantilever composite laminated shell subjected to a vertical force.

(a)

(b)

(c)
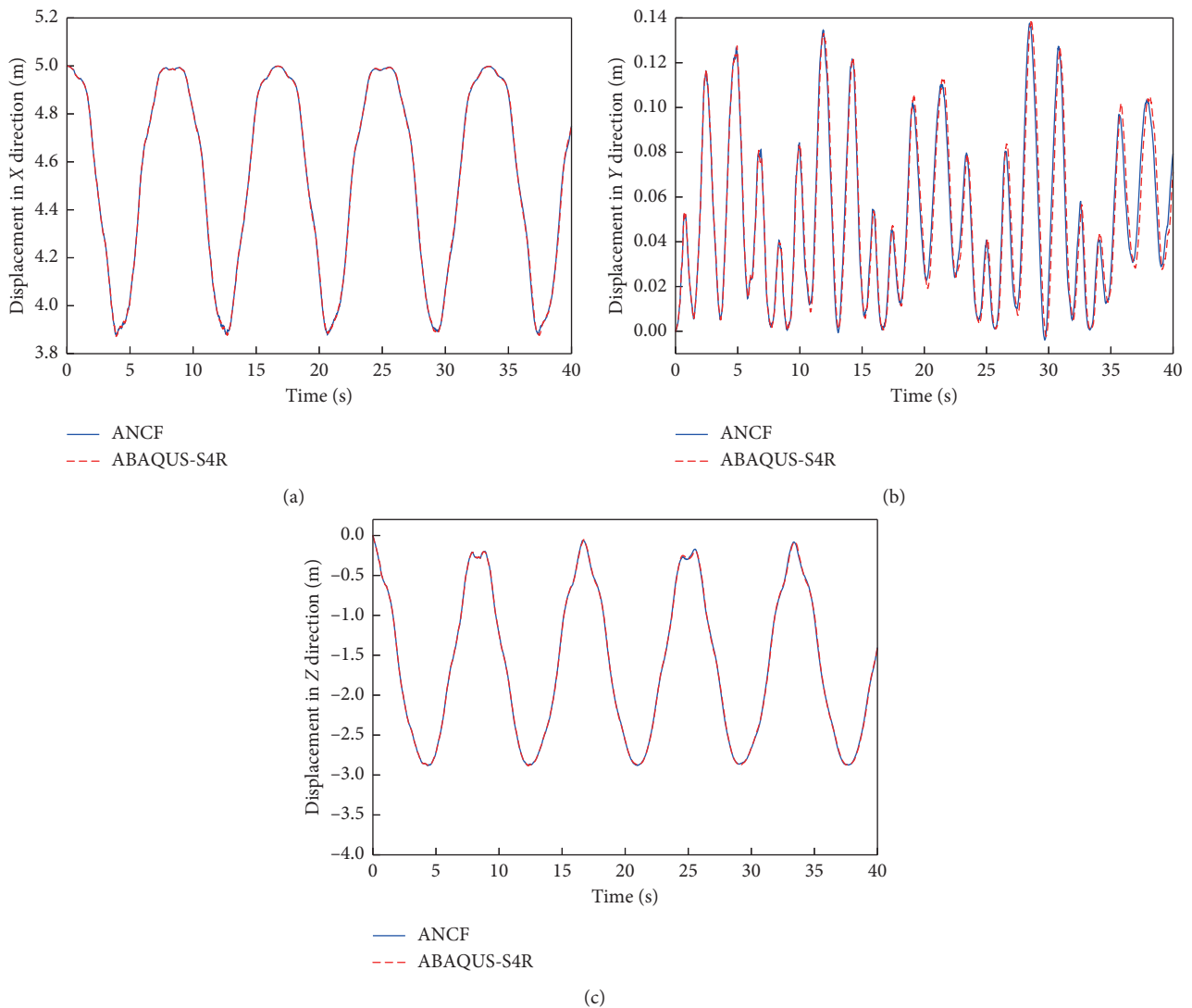
FIGURE 9: Displacement responses of the cantilever composite laminated shell.

torques gradually converge to zero during the deployment phase and reach a small neighbourhood of zero during the postlock phase. The driving torques of the two spring-dampers vary with the phases of the solar array deployment. Moreover, the torques of the two spring-dampers

still demonstrate a trend of obvious oscillations in the neighbourhood of zero in the postlock phase. However, the oscillations gradually decrease over time due to damping from the spring-dampers. Figure 12(b) illustrates the trends of synchronous control torque through

(a)

(b)
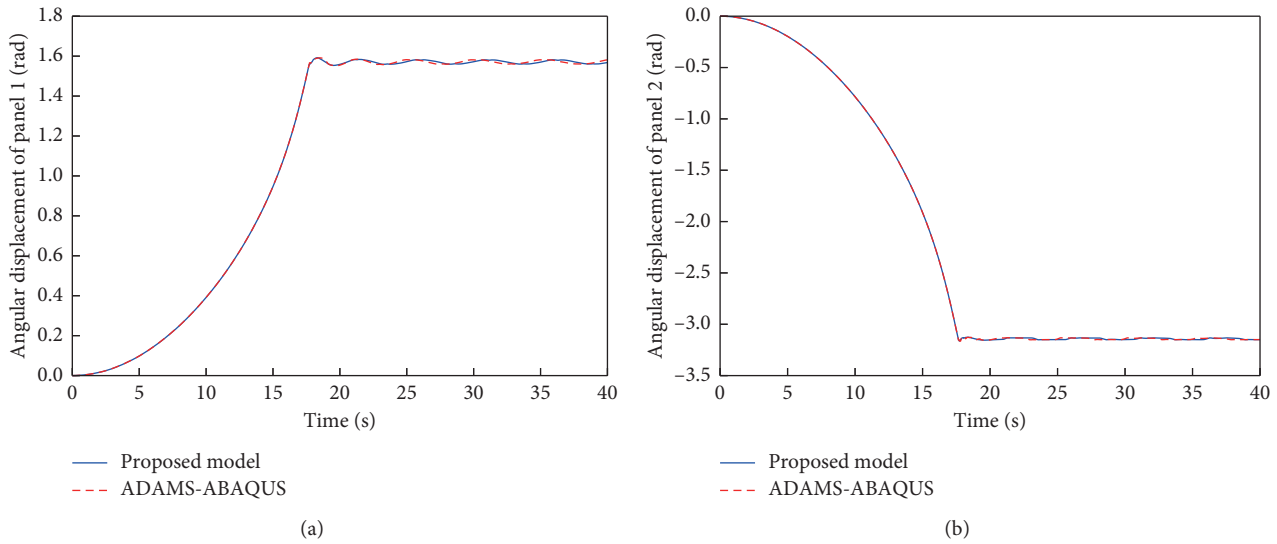
FIGURE 10: Comparison results of angular displacements of two solar panels between the proposed method and cosimulation of ADAMS-ABAQUS software.

(a)

(b)
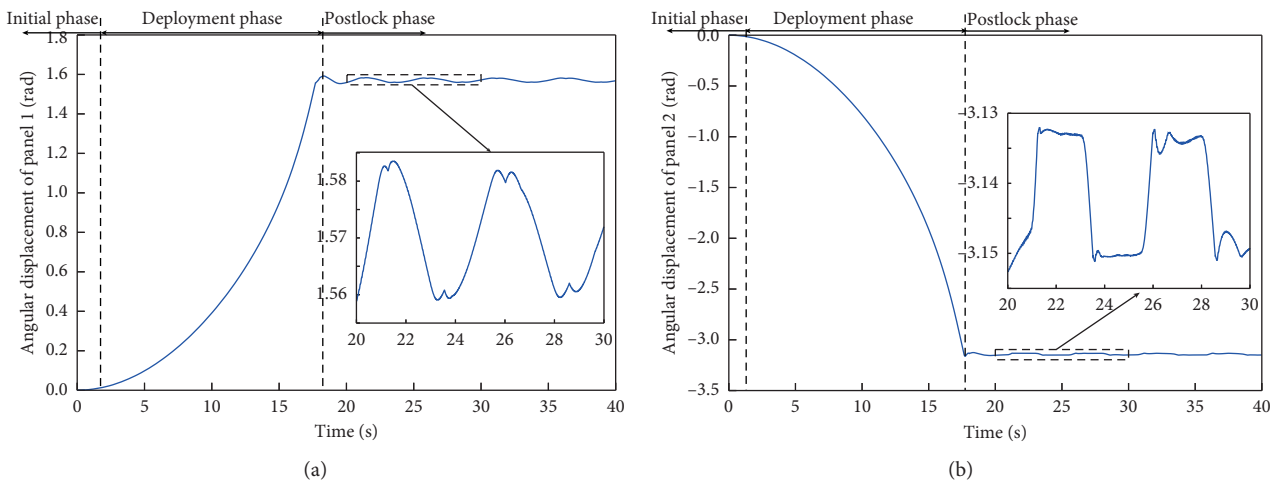
FIGURE 11: Angular displacements of two solar panels.

the CCL mechanism. The control torques of the two CCL mechanisms increase with small fluctuations in the early deployment phase and then reach the larger fluctuations in the later deployment phase. Figure 12(b) indicates that greater control torques produced from the CCL mechanism are required when the first panel becomes more out of sync with the second panel. After the two panels are locked, the control torques fluctuate around the domain of zero, indicating asynchronous oscillations within the two panels. The lock torque curves from the latch mechanism are illustrated in Figure 12(c). These results show that impulsive forces are induced when the locking operation is performed to lock the panels in a proper position. These impulsive forces are generally much larger than those from the other two mechanism types, which can lead to strong vibrations in the solar panels and may also cause the position deviations and attitude changes of the spacecraft main body. Moreover, the impulsive forces of the second latch mechanism are much

greater than those of the first latch mechanism. Therefore, several methods should be applied to avoid excessive impulsive forces from the latch mechanism.

Figure 13 presents the displacement responses of the main body during the deployment of the solar array. As shown in Figures 13(a), 13(b), and 13(c), the main body gradually deviates from its original position during the deployment phase. Moreover, the displacements of the main body in the X and Y directions are much larger than those in the Z direction. On the other hand, it is also shown in Figures 13(a) and 13(b) that the deviations climb to the top and remain steady in the postlock phase. The results demonstrate that the deployment of the solar array mainly causes the position deviations in the X and Y directions in the deployment phase. Therefore, the position changes in the X and Y directions are the main considerations in the controller design, while the change in Z direction is negligible.

(a)

(b)

(c)
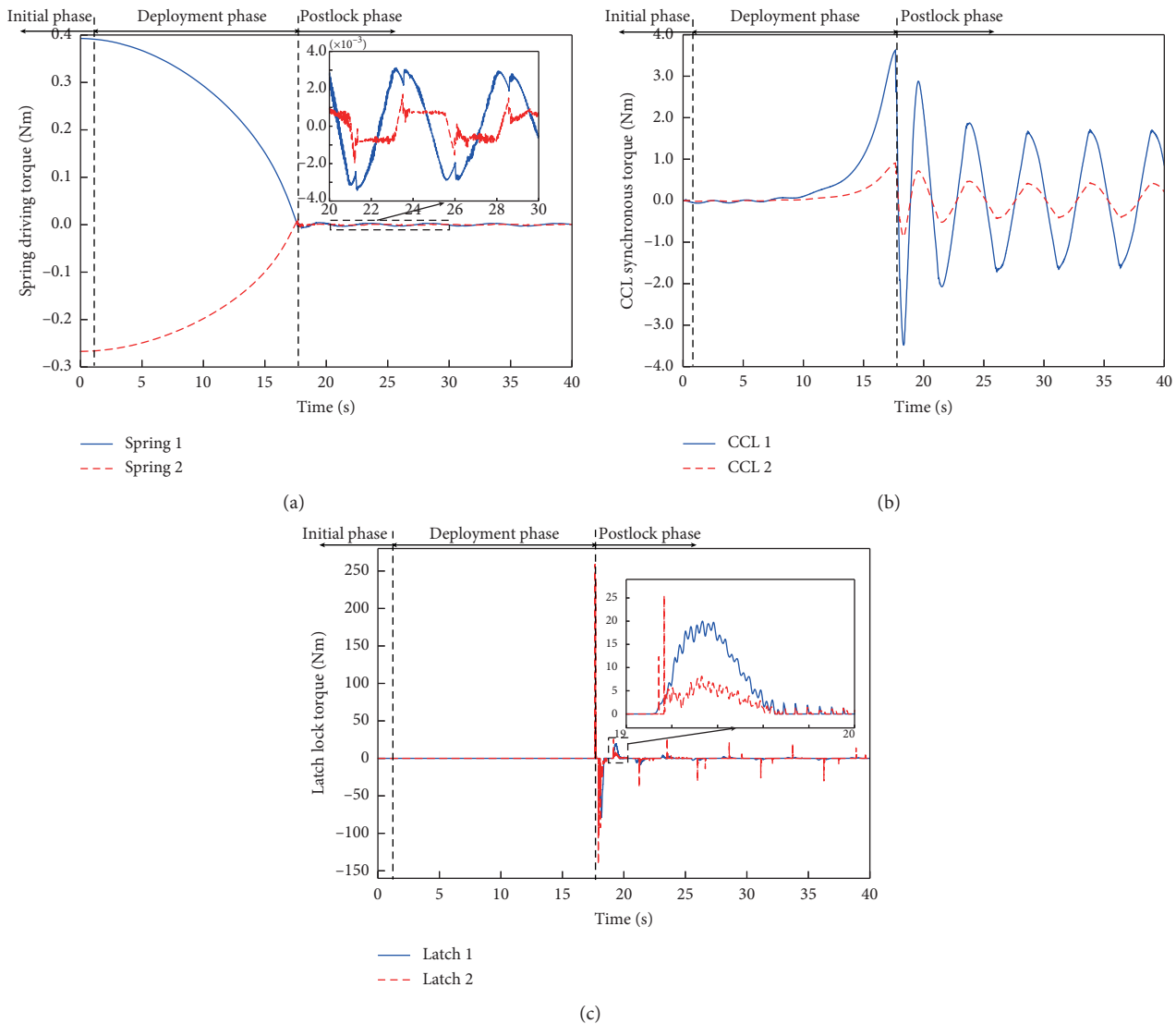
FIGURE 12: Torque responses of the solar array mechanisms.

Figure 14 illustrates the velocity responses of the main body during the deployment of solar arrays. The reference line in the following figures indicates that the value always keeps zero. As shown in Figure 14(a), the velocity signal gradually increases in the first 15 seconds and then decreases dramatically along the X direction throughout the deployment phase. From the zoomed part in Figure 14(a), there is a minor fluctuation in the postlock phase. As is illustrated in Figure 14(b), the velocity of the spacecraft main body increases steadily in the Y direction during the deployment phase and reaches a peak of 0.8×10^{-3} m/s. This decreases significantly after the solar panels are locked by the latch mechanisms. The velocity in the Y direction oscillates at a higher amplitude than it does in the X direction during the postlocking phase. The velocity in the Z direction is five orders of magnitude lower compared with that in the other two directions (see Figure 14(c)). Velocities in the X and Y

directions are therefore more significant in the controller design.

Figure 15 reveals the attitude responses of the main body during the deployment of the solar array system. As demonstrated in Figure 15(a), the rotation vector of the main body is almost constant with values (0.0, 0.0, 1.0) during all phases, which indicates that the main body approximately rotates around the Z axis during the deployment of solar arrays. As illustrated in Figures 15(b) and 15(c), the rotation angle and angular velocity of the main body have similar change tendencies during the deployment phase and reach the highest peak when the latch mechanisms lock the solar panels. After the solar panels are locked, the rotation angle and velocity of the main body present obvious fluctuations. Consequently, the rotation angle and velocity around the Z axis are indispensable variables to be taken into account in the controller design.

(a)

(b)

(c)
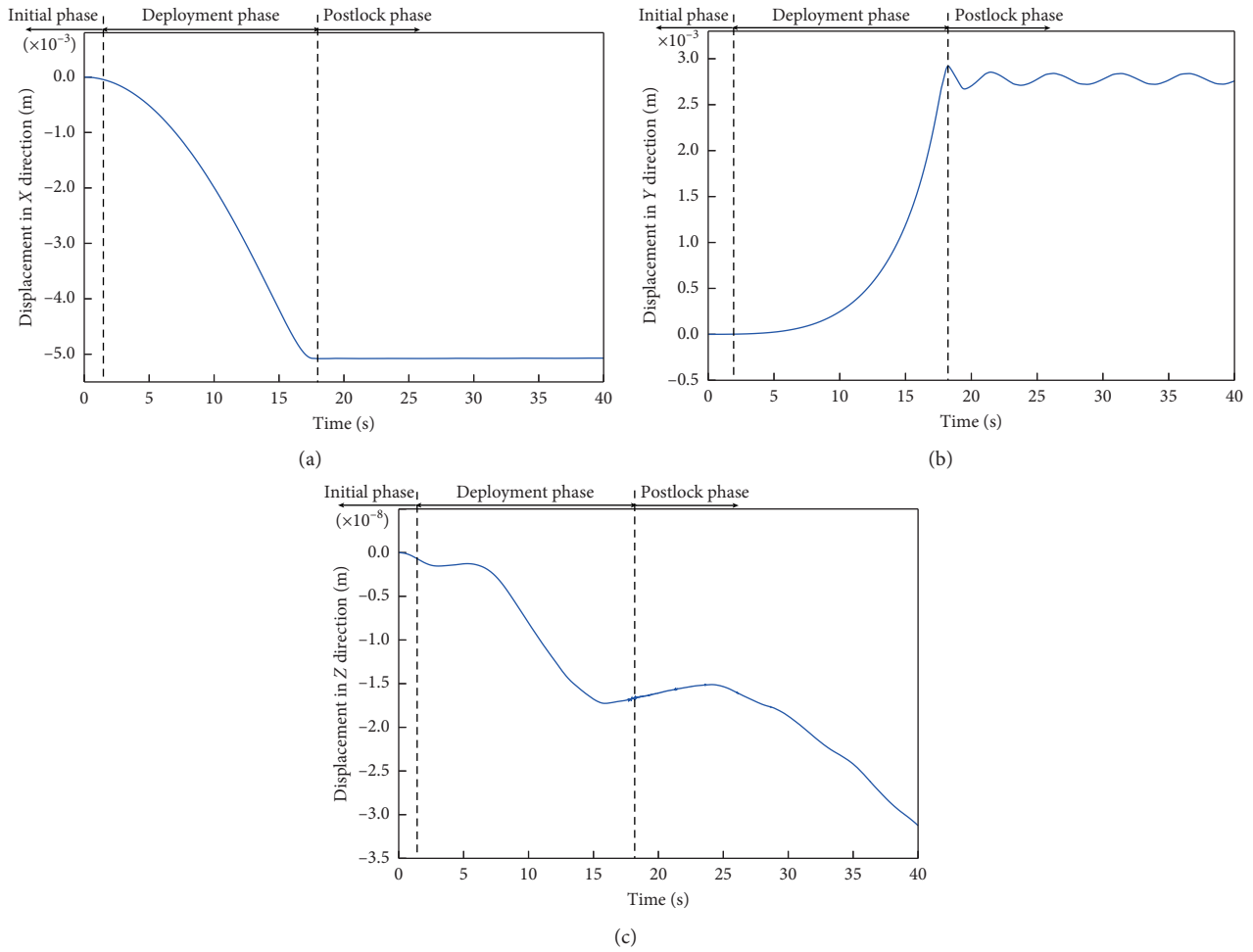
FIGURE 13: Displacement responses of the spacecraft main body in the three directions.

6.4. Conventional PD Control Scheme. The subsection presents a conventional PD control scheme to eliminate the position deviations and attitude changes of the spacecraft main body. As mentioned in the previous sections, the position deviations (X and Y directions) and attitude change (rotation around the Z axis) are major considerations in the control design. The desired displacements $\begin{bmatrix} r_{d,x} & r_{d,y} \end{bmatrix}$ and velocities $\begin{bmatrix} \dot{r}_{d,x} & \dot{r}_{d,y} \end{bmatrix}$ in equation (43), the desired rotation angle γ, and angular velocity $w_{d,z}$ in equation (45) are set to be zero. Two groups of the simulation cases were preformed to investigate the effects of the PD parameters on the control performance. The parameters of these simulation cases are listed in Table 2. Figure 16 depicts the evolution of the position and attitude responses of the spacecraft in these simulation cases.

Figure 16 shows that all the state variables of the spacecraft main body converge nearly to zero, indicating that the spacecraft system is stabilized successfully under the conventional PD control scheme. In Group 1, the differential gain K_D is fixed, while the proportional gain K_P gradually increases in these simulation cases. As illustrated in Figures 16(a) and 16(c), the displacement deviations of the spacecraft in the X and Y directions significantly decrease and expedite the convergence to zero with the increase of the

proportional gain K_P. The attitudes of the spacecraft are also obviously stabilized as shown in Figure 16(e). The proportional term of the PD controller provides an overall control action proportional to the error signals through the gain factor, which means that the steady-state error and rise time of the system reduced by increasing the proportional gain factor. However, an increase in the proportional gain factor also decreases the stability margins and may induce oscillations in the system. It is insufficient to use only the proportional gain factor to improve the system responses. In Group 2, the proportional gain K_P is fixed, while the differential gain K_D increases in order to evaluate the effects of the differential term of the PD controller. As depicted in Figures 16(b) and 16(d), the displacement responses of the spacecraft in the X and Y directions have been improved to a certain extent with the increase of the differential gain K_D. After the solar panels are locked, the rotation angle of the spacecraft has obvious fluctuations. From the zoomed part in Figure 16(f), the amplitude of these fluctuations significantly decreases with the increase of the differential gain K_D. The differential term of the PD controller is capable of predicting the trend of error signals and thus improving the transient responses and system stability through high-frequency compensation. However, the differential term of the
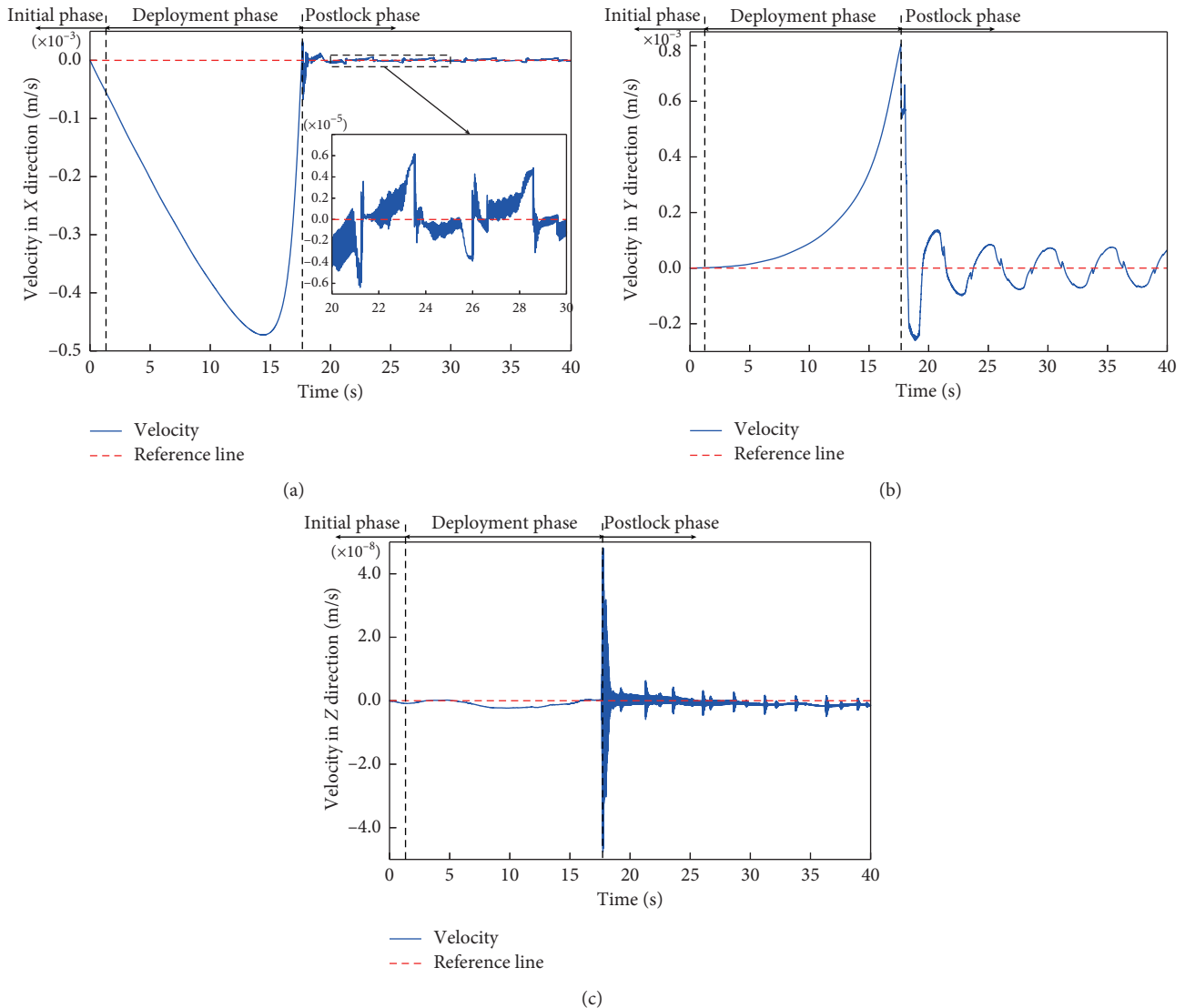
Figure 14: Velocity responses of the spacecraft main body in the three directions.

PD controller is sensitive to the interference noises of the system. The improper differential gain factor is likely to reduce the ability to suppress the interference noises. Therefore, the proportional and differential terms of the PD controller must be tuned jointly for optimum performance. An online adjustment for the PD controller is required to stabilize the spacecraft.

6.5. Adaptive Fuzzy PD Control Scheme. As discussed in the previous subsection, the conventional PD controller can stabilize the spacecraft system successfully. However, the parameters of the PD controller cannot be accurately determined in the presence of uncertainty and nonlinearity within the spacecraft system. This subsection presents an adaptive fuzzy PD control scheme. According to the discussion about the effects of the PD control parameters on the control performance in the previous section, we designed the fuzzy rules of the fuzzy PD controller as listed in Table 3 [4].

The membership functions were chosen to be triangular and *S*-shaped, due to their simplicity and sensitivity to small variations. Figure 17 shows these membership functions chosen for both inputs and outputs of each fuzzy tuner. Figures 17(a) and 17(c) depict the membership functions of the fuzzy tuner to characterize the position errors in the *X* and *Y* directions, respectively, and Figure 17(e) illustrates the membership functions to deal with attitude angle errors. Figures 17(b), 17(d), and 17(f) show the corresponding membership functions for the velocity errors. Figures 17(g) and 17(h) depict the membership functions for the increments of the proportional and differential gains, respectively.

Figure 18 compares the position and attitude responses between the fuzzy PD control scheme and the conventional PD control scheme. As shown in Figures 18(a) and 18(c), the position deviations of the spacecraft main body in the *X* and *Y* directions for the fuzzy PD controller are generally less than those for the

(a)

(b)

(c)
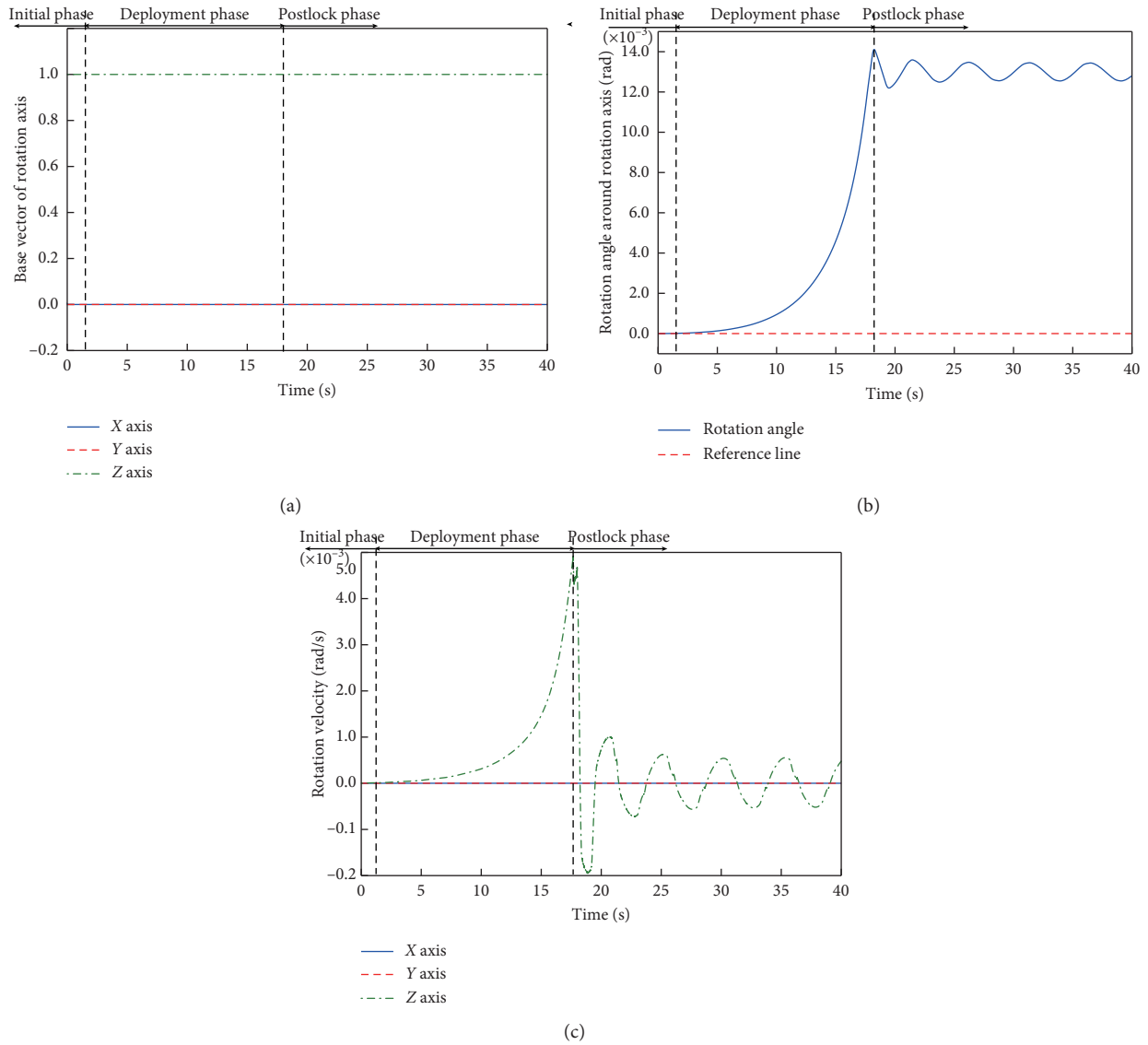
FIGURE 15: Attitude responses of the spacecraft main body.

TABLE 2: Parameters of the PD controller in the simulation cases.

Group list	Case list	K_P	K_D
	Case 1	6.5	12.5
Group 1	Case 2	12.0	12.5
	Case 3	17.0	12.5
	Case 1	17.0	5.5
Group 2	Case 2	17.0	12.5
	Case 3	17.0	25.6

conventional PD control scheme. The conventional PD controller requires about 30 s to successfully stabilize the spacecraft system in the X direction, while this takes about 20 s for the fuzzy PD controller. In the Y direction, the spacecraft main body presents obvious fluctuations after

the solar array is locked and requires more time than the X direction to stabilize. The amplitude of these fluctuations for the fuzzy PD controller is generally smaller than those for the conventional PD controller. As depicted in Figures 18(b) and 18(d), the spacecraft's velocities fluctuate near the zero values, of which the amplitude under the fuzzy PD control is smaller than that under the conventional PD control. The results indicate that the position responses of the spacecraft main body under the fuzzy PD control are significantly improved in comparison with those under the conventional PD control. Figures 18(e) and 18(f) illustrate the contrast of the attitude responses between the fuzzy PD control and the conventional PD control. To reveal the details, the rotation angles in the deployment phase are zoomed, where the rotation angles under the fuzzy PD control are shown
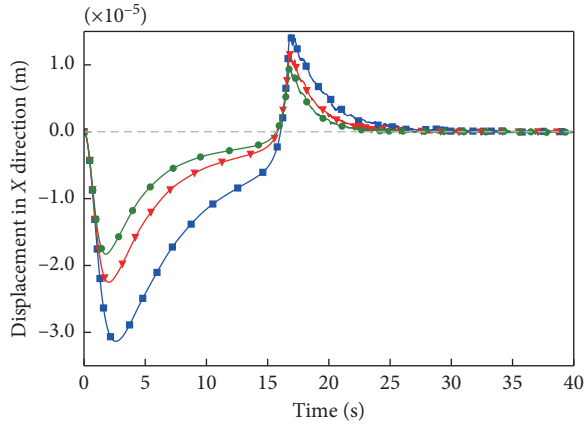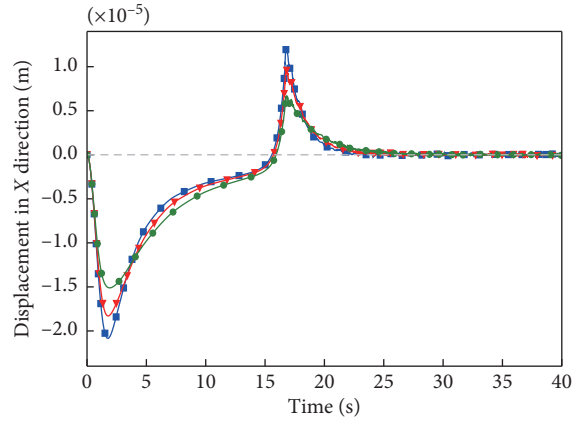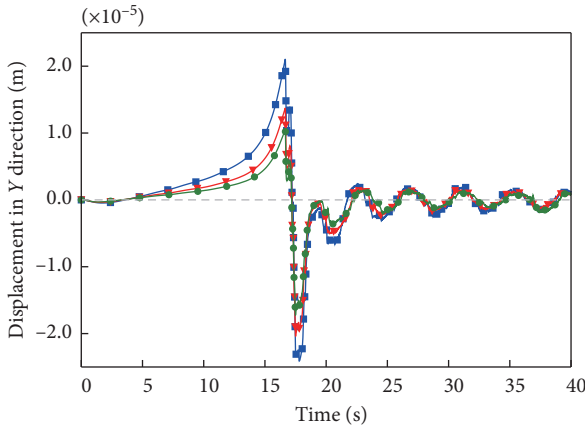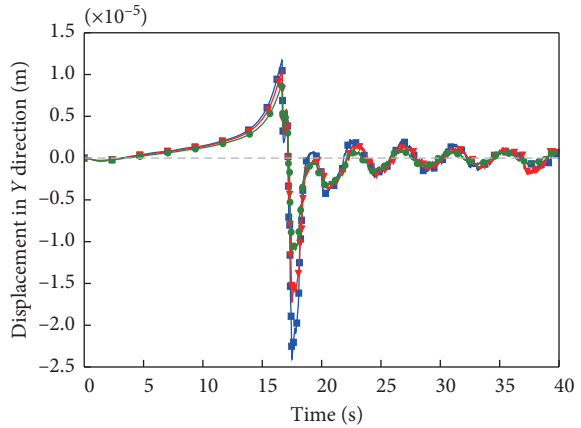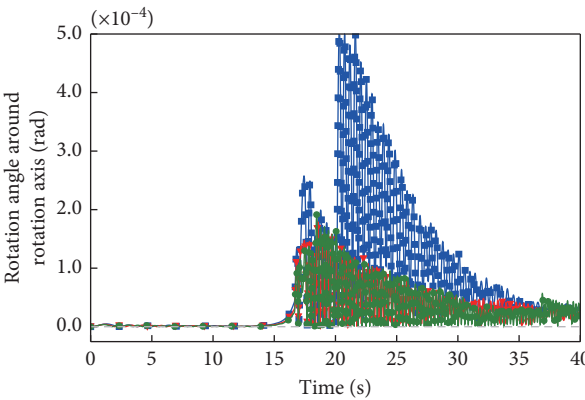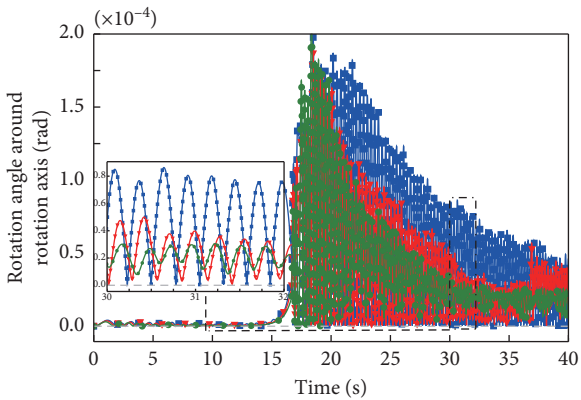
FIGURE 16: Position and attitude responses of the spacecraft varying with PD controller parameters.

TABLE 3: Fuzzy rules of the fuzzy PD controller.

Rule index	Rule statements
Rule 1	If (E is N) and (EC is N), then (ΔK_P is P) and (ΔK_D is P)
Rule 2	If (E is N) and (EC is Z), then (ΔK_P is P) and (ΔK_D is Z)
Rule 3	If (E is N) and (EC is P), then (ΔK_P is N) and (ΔK_D is P)
Rule 4	If (E is Z) and (EC is N), then (ΔK_P is Z) and (ΔK_D is P)
Rule 5	If (E is Z) and (EC is Z), then (ΔK_P is Z) and (ΔK_D is Z)
Rule 6	If (E is Z) and (EC is P), then (ΔK_P is Z) and (ΔK_D is P)
Rule 7	If (E is P) and (EC is N), then (ΔK_P is N) and (ΔK_D is P)
Rule 8	If (E is P) and (EC is Z), then (ΔK_P is P) and (ΔK_D is Z)
Rule 9	If (E is P) and (EC is P), then (ΔK_P is P) and (ΔK_D is P)

(a)

(b)

(c)

(d)

(e)

(f)
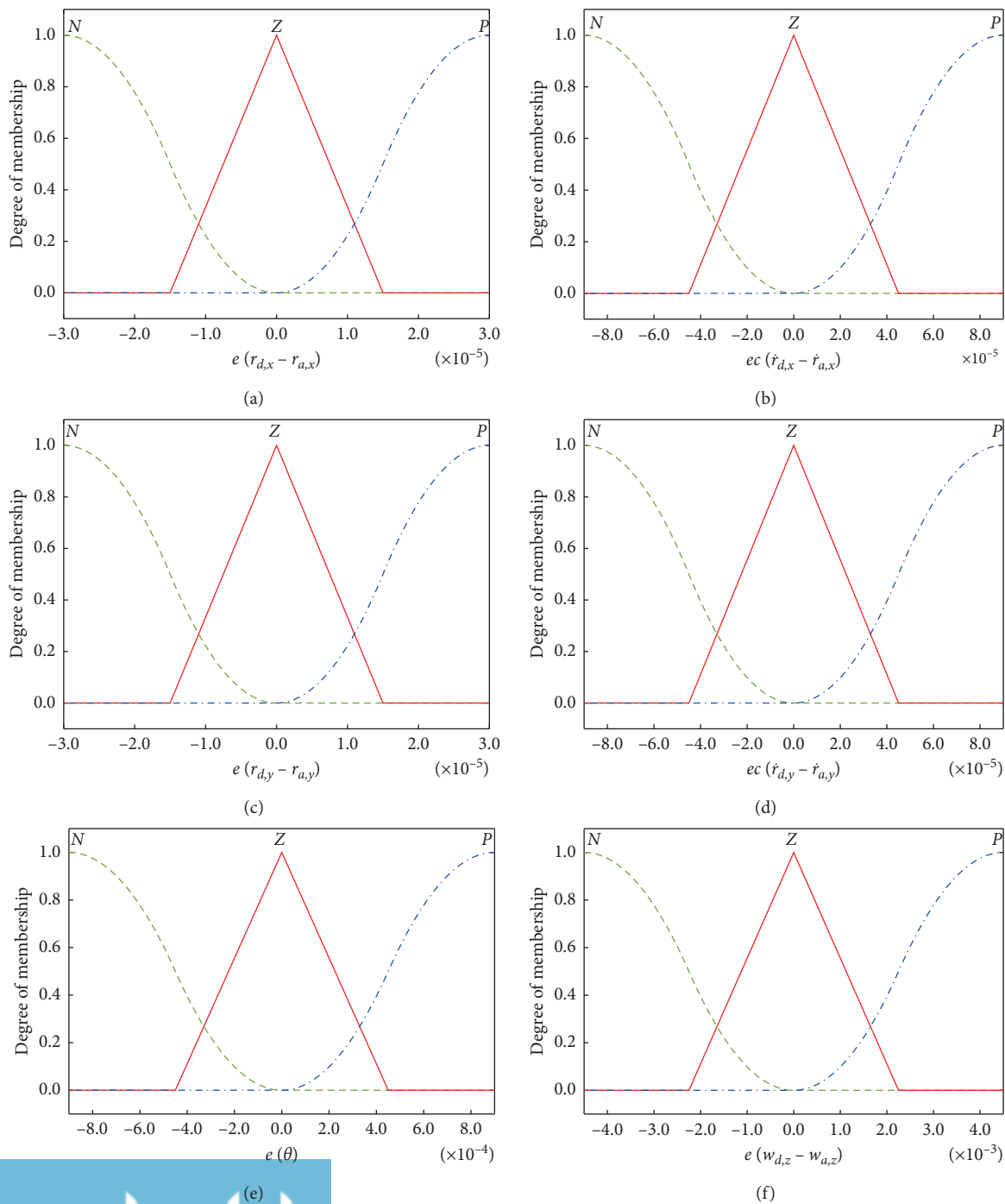
FIGURE 17: Continued.
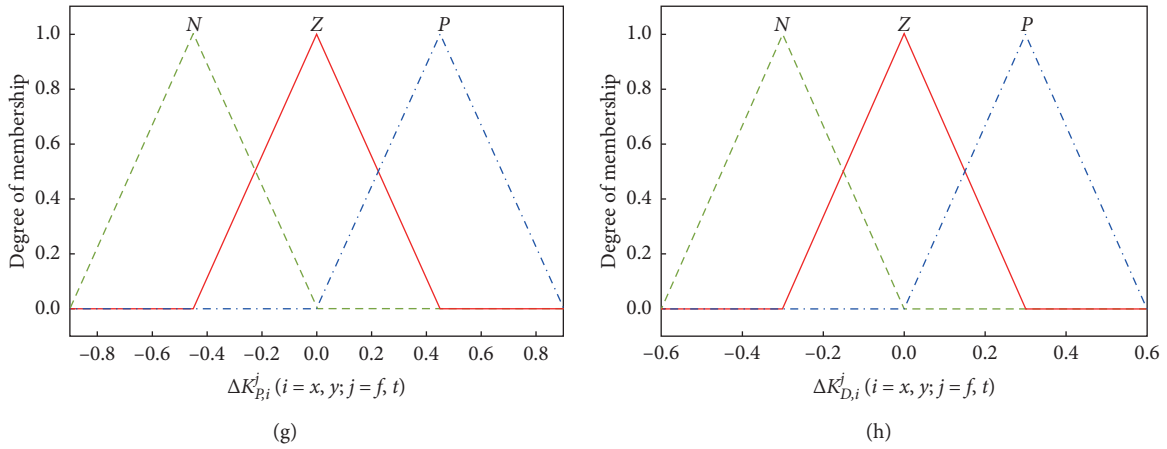
Figure 17: Membership functions (MFs) chosen for both inputs and outputs of each fuzzy tuner.

(a)

(b)

(c)

(d)
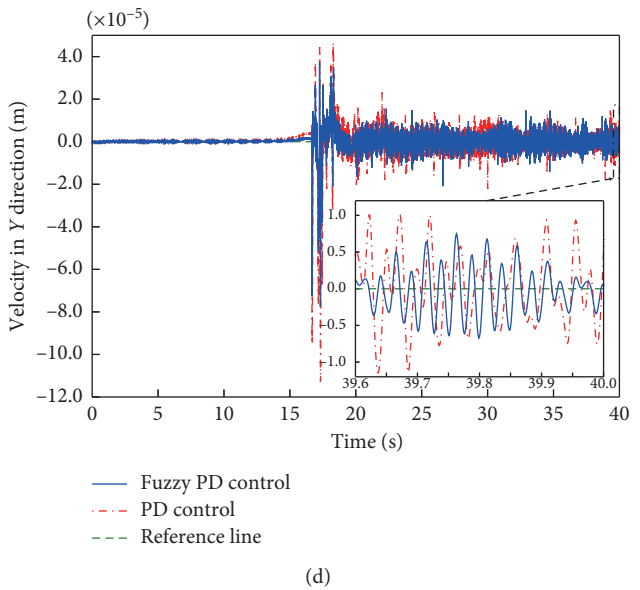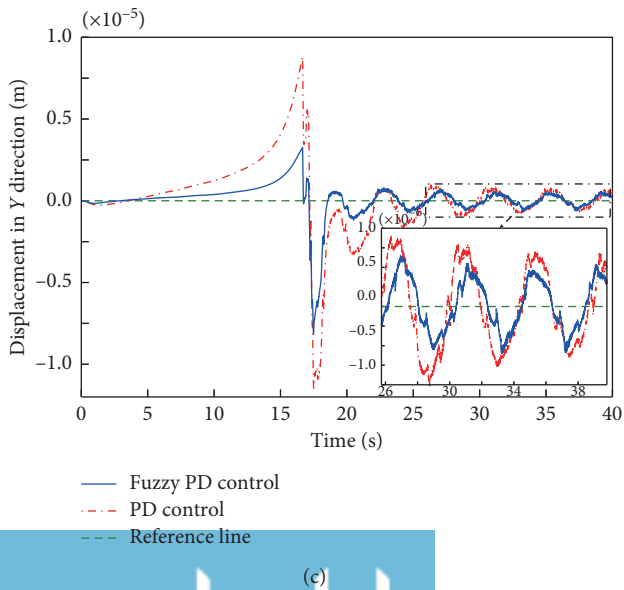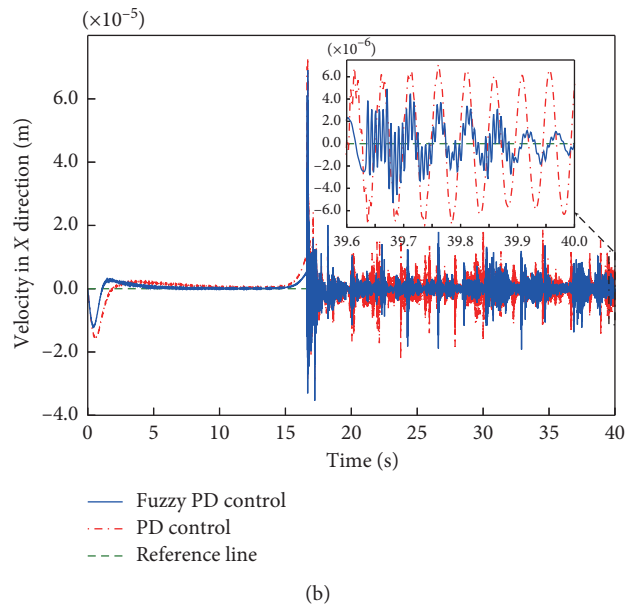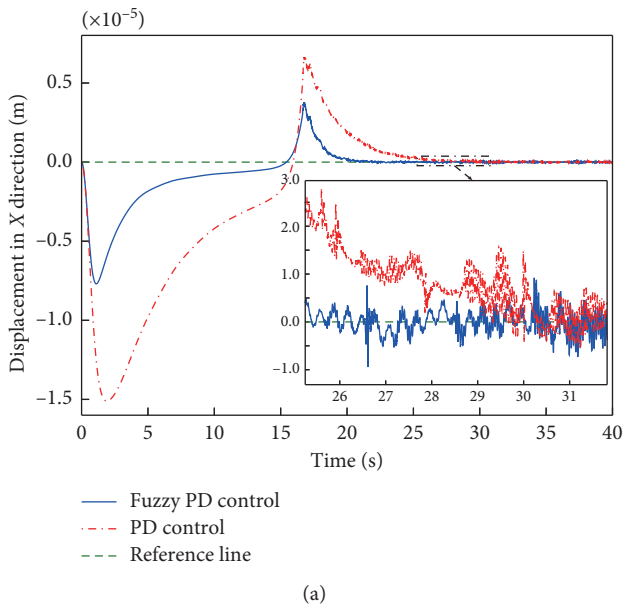
Figure 18: Continued.
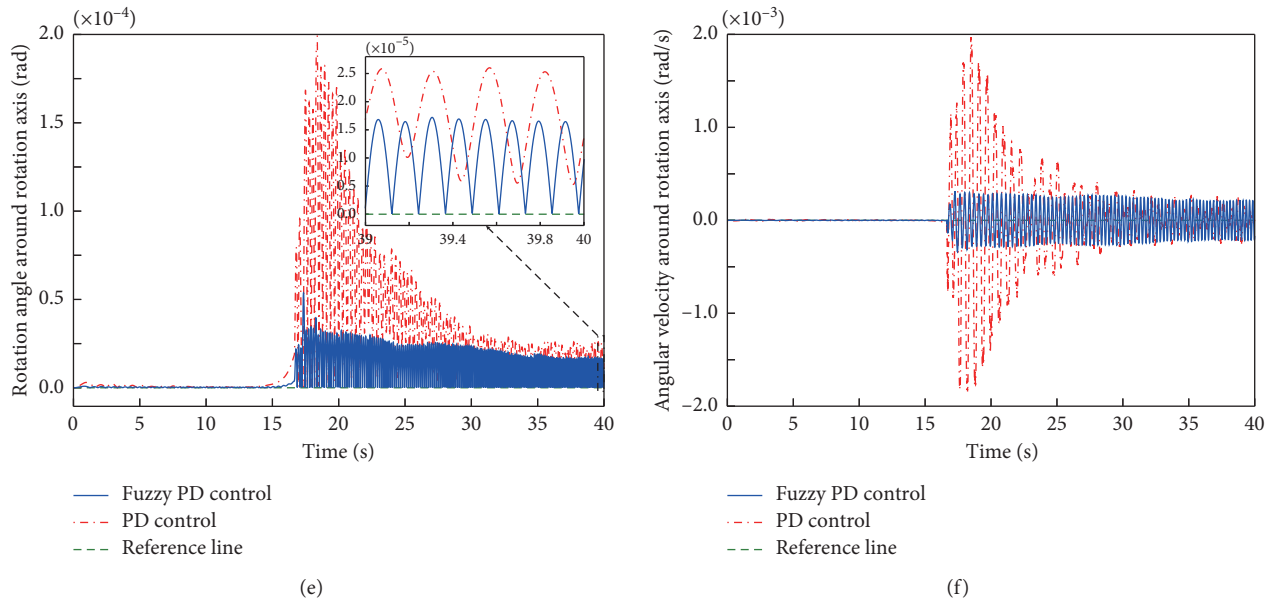
FIGURE 18: Comparisons of position and attitude responses between fuzzy PD control and conventional PD control.

to be smaller than those under the conventional PD control. When the solar panels are locked, the rotation angles of the spacecraft suddenly increase as the result of the induced impulsive forces generated from the latch mechanisms. After that, the rotation angles of the spacecraft with the fuzzy PD controller converge to zero faster than those with the conventional PD controller. The angular velocities of the spacecraft follow the similar trends. The results indicate that the fuzzy PD controller is more robust than the conventional PD controller in terms of the attitude stabilization of the spacecraft.

The adaptive fuzzy control scheme has much better performance in terms of the control precision and time response, especially in complex systems with uncertainties. Similar conclusions were also reported by previous studies. Yang et al. [68] proposed an adaptive fuzzy control scheme for coordinated robot arms in the presence of system uncertainties and compared it with a model-based controller and a conventional PD controller. The comparisons have shown that the adaptive fuzzy controller obtained the best control performance and the lowest tracking errors. Najafizadeh et al. [52] designed an adaptive fuzzy PID controller for the attitude control of the geostationary satellite. The results have shown that the adaptive fuzzy PID controller can achieve faster convergence time and higher performance. Calvo et al. [49] developed a fuzzy controller for attitude control of a satellite and compared it with the PID controller. The comparisons have proved that the fuzzy controller has superior performance on the control precision. In recent years, a versatile intelligent control scheme has appeared and performed better under the uncertainties condition. Yang et al. [69] developed a neural network-based controller to track the generated motions of a robot. Tsai et al. [32] combined the fuzzy wavelet neural networks with a

novel adaptive predictive PID control for a kind of highly nonlinear discrete-time system with time delay. In the future work, we will attempt to combine the more intelligent techniques with the classical control scheme to improve the dynamic responses of the flexible spacecraft with uncertainties and nonlinearities.

7. Conclusions

This paper presented a novel adaptive control scheme, which combines the fuzzy logic technique and PD control for attitude stabilization of a flexible spacecraft during the deployment of the solar array. The dynamic model of a constrained rigid-flexible coupling spacecraft system with a composite laminated solar array was first proposed. The validity of our dynamic model was verified by comparing with the cosimulation of the ADAMS-ABAQUS software. The comparison results showed that the proposed model can adequately describe the deployment dynamics of a solar array that composed of composite laminated shells. The dynamic responses of the spacecraft during the deployment of the solar array were then investigated. The deployment of the composite laminated solar array mainly causes the position deviations in X and Y directions, as well as the spacecraft main body approximately rotating around the Z axis. Moreover, a control scheme for attitude stabilization of the flexible spacecraft was proposed. The parameters of a PD controller play an evident role in the control performance for improving the displacement and attitude responses of the spacecraft. However, these parameters cannot be accurately determined. The effectiveness of the proposed adaptive fuzzy PD control scheme was evaluated by comparing with that of the conventional PD controllers. The comparison results revealed the superiorities of the proposed adaptive fuzzy

PD controller over the conventional PD controller. The results further provide inspiration for the design of control strategies for complex spacecraft with uncertainty and nonlinearity.

Appendix

A. Virtual Work for Inertial Force and External Force

Assuming that the point Q is associated with an infinitesimal mass element $\mathrm{d}m$, the virtual work done by the inertial force can be expressed as

$$
\begin{aligned}
\delta W_{\mathrm{ine}}^{b} &= -\int_{m} \left(\delta r_{Q}\right)^{\mathrm{T}} \ddot{r}_{Q} \mathrm{d}m, \\
&= -\int_{m} \left(\delta r^{\mathrm{T}} + \delta \pi^{\mathrm{T}} \widetilde{s}' A^{\mathrm{T}}\right) \left(\ddot{r} + A \widetilde{\dot{\omega}} s' + A \widetilde{\omega} \widetilde{\omega} s'\right) \mathrm{d}m, \\
&= -\delta r^{\mathrm{T}} \ddot{r} \int_{m} \mathrm{d}m - \delta r^{\mathrm{T}} \left(A \widetilde{\dot{\omega}} + A \widetilde{\omega} \widetilde{\omega}\right) \int_{m} s' \mathrm{d}m - \delta \pi^{\mathrm{T}} \\
&\quad \int_{m} s' \mathrm{d}m A^{\mathrm{T}} \ddot{r} - \delta \pi^{\mathrm{T}} \int_{m} \widetilde{s}' \widetilde{\dot{\omega}} s' \mathrm{d}m - \delta \pi^{\mathrm{T}} \int_{m} \widetilde{s}' \widetilde{\omega} \widetilde{\omega} s' \mathrm{d}m.
\end{aligned}
\tag{A.1}
$$

If an external force f (per unit mass) act at point Q, the virtual work done by the external force can be obtained by

$$
\begin{aligned}
\delta W_{\mathrm{ext}}^{b} &= \int_{m} \delta \left(r^{P}\right)^{\mathrm{T}} f \mathrm{d}m, \\
&= \int_{m} \left(\delta r^{\mathrm{T}} + \delta \pi^{\mathrm{T}} \widetilde{s}' A^{\mathrm{T}}\right) f \mathrm{d}m, \\
&= \delta r^{\mathrm{T}} \int_{m} f \, \mathrm{d}m + \delta \pi^{\mathrm{T}} \int_{m} \widetilde{s}' A^{\mathrm{T}} f \mathrm{d}m, \\
&= \delta r^{\mathrm{T}} \int_{m} f \, \mathrm{d}m + \delta \pi^{\mathrm{T}} \int_{m} \widetilde{s}' f \prime \mathrm{d}m.
\end{aligned}
\tag{A.2}
$$

Since the origin of the local coordinate frame x-y-z is located at the center of mass of the body, the total mass of the body can be expressed as

$$
m = \int_{m} \mathrm{d}m.
\tag{A.3}
$$

The total external force is acting on the body with the following expression:

$$
F_{b} = \int_{m} f \mathrm{d}m.
\tag{A.4}
$$

The torque of the external forces with respect to the origin of the local coordinate frame is

$$
n = \int_{m} \widetilde{s}' f \mathrm{d}m.
\tag{A.5}
$$

The constant inertia tensor can be defined as

$$
J = -\int_{m} \widetilde{s}' \widetilde{s}' \mathrm{d}m = \int_{m} \begin{bmatrix} y^{2} + z^{2} & -xy & -xz \\ -xy & x^{2} + z^{2} & -yz \\ -xy & -yz & x^{2} + y^{2} \end{bmatrix} \mathrm{d}m.
\tag{A.6}
$$

And the following mathematical relation satisfies

$$
\int_{m} s' \mathrm{d}m = 0.
\tag{A.7}
$$

Substituting (A.3), (A.6), and (A.7) into (A.1) yields

$$
\delta W_{\mathrm{ine}}^{b} = -\delta r^{\mathrm{T}} m \ddot{r} - \delta \pi^{\mathrm{T}} J \dot{\omega} - \delta \pi^{\mathrm{T}} \widetilde{\omega} J \widetilde{\omega}.
\tag{A.8}
$$

Substituting (A.4) and (A.5) into (A.2) yields

$$
\delta W_{\mathrm{ext}}^{b} = \delta r^{\mathrm{T}} F_{b} + \delta \pi^{\mathrm{T}} n.
\tag{A.9}
$$

Using (8) and (12), the following expression can be obtained as

$$
\begin{aligned}
\dot{\omega} &= 2G \ddot{p}, \\
\widetilde{\omega} &= 2G \dot{G}^{\mathrm{T}}, \\
\delta \pi &= 2G^{\mathrm{T}} \delta p.
\end{aligned}
\tag{A.10}
$$

Then, (A.8) can be rewritten as

$$
\delta W_{\mathrm{ine}}^{b} = -\delta r^{\mathrm{T}} m \ddot{r} - \delta p^{\mathrm{T}} \left(4G^{\mathrm{T}} J G \ddot{p} - 8 \dot{G}^{\mathrm{T}} J \dot{G} p\right).
\tag{A.11}
$$

And (A.9) can be rewritten as

$$
\delta W_{\mathrm{ext}}^{b} = \delta r^{\mathrm{T}} F_{b} + \delta p^{\mathrm{T}} \left(2G^{\mathrm{T}} n\right).
\tag{A.12}
$$

B. Saint Venant–Kirchhoff Material Model

With regard to the orthotropic Saint Venant–Kirchhoff nonlinear material, the second Piola–Kirchhoff stress can be expressed as

$$
S = \frac{\partial W}{\partial \varepsilon} = C : \varepsilon,
\tag{B.1}
$$

where C is the fourth-order material modulus. The material modulus can be defined as [70]

$$
C^{ijkl} = \left(b^{i} \cdot a_{a}\right) \left(b^{j} \cdot a_{b}\right) \left(b^{k} \cdot a_{c}\right) \left(b^{l} \cdot a_{d}\right) \overline{C}^{abcd},
\tag{B.2}
$$

where $\{a_{1} \, a_{2} \, a_{3}\}$ is the fiber coordinate frame, $\{b^{1} \, b^{2} \, b^{3}\}$ is the global coordinate frame, and $\overline{C}^{abcd}$ is the tangent material modulus in the fiber coordinate frame. The tangent material modulus can be defined as

$$
\left[\overline{C}^{abcd}\right] = \begin{bmatrix} \overline{C}^{1111} & \overline{C}^{1122} & 0 & \overline{C}^{1133} & 0 & 0 \\ \overline{C}^{1122} & \overline{C}^{2222} & 0 & \overline{C}^{2233} & 0 & 0 \\ 0 & 0 & \overline{C}^{1212} & 0 & 0 & 0 \\ \overline{C}^{1133} & \overline{C}^{2233} & 0 & \overline{C}^{3333} & 0 & 0 \\ 0 & 0 & 0 & 0 & \overline{C}^{2323} & 0 \\ 0 & 0 & 0 & 0 & 0 & \overline{C}^{1313} \end{bmatrix},
\tag{B.3}
$$

where

$$\overline{C}^{1111} = \frac{E_1\left(1 - \nu_{23}\nu_{32}\right)}{\Delta} \qquad \overline{C}^{2222} = \frac{E_2\left(1 - \nu_{13}\nu_{31}\right)}{\Delta} \qquad \overline{C}^{3333} = \frac{E_3\left(1 - \nu_{12}\nu_{21}\right)}{\Delta}$$

$$\overline{C}^{1122} = \frac{E_1\left(\nu_{21} + \nu_{31}\nu_{23}\right)}{\Delta} \qquad \overline{C}^{1133} = \frac{E_3\left(\nu_{13} + \nu_{12}\nu_{23}\right)}{\Delta} \qquad \overline{C}^{2233} = \frac{E_2\left(\nu_{32} + \nu_{12}\nu_{31}\right)}{\Delta} \qquad \text{(B.4)}$$

$$\overline{C}^{1212} = G_{12} \qquad\qquad \overline{C}^{2323} = G_{23} \qquad\qquad \overline{C}^{1313} = G_{13}$$

$$\Delta = 1 - \nu_{12}\nu_{21} - \nu_{23}\nu_{32} - \nu_{31}\nu_{13} - 2\nu_{21}\nu_{32}\nu_{13}$$

where E_1, E_2, and E_3 are Young's moduli; G_1, G_2, and G_3 are the shear moduli; and ν_{12}, ν_{13}, ν_{23}, ν_{21}, ν_{31}, and ν_{32} are Poisson's ratios.

Data Availability

The data used to support the findings of this study are available from the corresponding author upon request.

Conflicts of Interest

The authors declare that there are no conflicts of interest regarding the publication of this paper.

References

[1] S.-J. Guo, H.-Q. Li, and G.-P. Cai, "Deployment dynamics of a large-scale flexible solar array system on the ground," *The Journal of the Astronautical Sciences*, vol. 66, no. 3, pp. 225–246, 2019.

[2] A. Kote, K. Balaji, B. S. Nataraju, and V. C. Aralimatti, "Effect of solar array deployment on spacecraft attitude," *Journal of Spacecraft Technology*, vol. 17, pp. 1–8, 2007.

[3] Z. Bai and Y. Zhao, "Attitude motion of spacecraft during oblique solar panel deployment," *Aircraft Engineering and Aerospace Technology*, vol. 84, 2012.

[4] H.-Q. Li, X.-F. Liu, L.-C. Duan, and G.-P. Cai, "Deployment and control of spacecraft solar array considering joint stick-slip friction," *Aerospace Science and Technology*, vol. 42, pp. 342–352, 2015.

[5] A. Gloria, D. Ronca, T. Russo et al., "Technical features and criteria in designing fiber-reinforced composite materials: from the aerospace and aeronautical field to biomedical applications," *Journal of Applied Biomaterials & Biomechanics*, vol. 9, 2011.

[6] S. A. Emam and D. J. Inman, "A review on bistable composite laminates for morphing and energy harvesting," *Applied Mechanics Reviews*, vol. 67, 2015.

[7] B. Adhikari and B. N. Singh, "An efficient higher order non-polynomial Quasi 3-D theory for dynamic responses of laminated composite plates," *Composite Structures*, vol. 189, pp. 386–397, 2018.

[8] M. A. Neto, J. A. C. Ambr'osio, and R. e. P. Leal, "Flexible multibody systems models using composite materials components," *Multibody System Dynamics*, vol. 12, no. 4, pp. 385–405, 2004.

[9] M. A. Neto, J. A. C. Ambrósio, and R. P. Leal, "Composite materials in flexible multibody systems," *Computer Methods in Applied Mechanics and Engineering*, vol. 195, no. 50-51, pp. 6860–6873, 2006.

[10] J. A. C. Ambrósio, M. A. Neto, and R. P. Leal, "Optimization of a complex flexible multibody systems with composite materials," *Multibody System Dynamics*, vol. 18, no. 2, pp. 117–144, 2007.

[11] J. Gerstmayr, H. Sugiyama, and A. Mikkola, "Review on the absolute nodal coordinate formulation for large deformation analysis of multibody systems," *Journal of Computational and Nonlinear Dynamics*, vol. 8, pp. 31012–31016, 2013.

[12] A. A. Shabana, "Flexible multibody dynamics: review of past and recent developments," *Multibody System Dynamics*, vol. 1, no. 2, pp. 189–222, 1997.

[13] A. A. Shabana, "Definition of the slopes and the finite element absolute nodal coordinate formulation," *Multibody System Dynamics*, vol. 1, pp. 339–348, 1997.

[14] K. Nachbagauer, "State of the art of ANCF elements regarding geometric description, interpolation strategies, definition of elastic forces, validation and the locking phenomenon in comparison with proposed beam finite elements," *Archives of Computational Methods in Engineering*, vol. 21, no. 3, pp. 293–319, 2014.

[15] Y. Li, C. Wang, and W. Huang, "Dynamics analysis of planar rigid-flexible coupling deployable solar array system with multiple revolute clearance joints," *Mechanical Systems and Signal Processing*, vol. 117, pp. 188–209, 2019.

[16] Y. Li, C. Wang, and W. Huang, "Rigid-flexible-thermal analysis of planar composite solar array with clearance joint considering torsional spring, latch mechanism and attitude controller," *Nonlinear Dynamics*, vol. 96, 2019.

[17] C. Liu, Q. Tian, and H. Hu, "Dynamics of a large scale rigid-flexible multibody system composed of composite laminated plates," *Multibody System Dynamics*, vol. 26, no. 3, pp. 283–305, 2011.

[18] K. H. Ang, G. Chong, and Y. Li, "PID control system analysis, design, and technology," *IEEE Transactions on Control Systems Technology*, vol. 13, pp. 559–576, 2005.

[19] M. S. Can and O. F. Ozguven, "PID tuning with neutrosophic similarity measure," *International Journal of Fuzzy Systems*, vol. 19, 2017.

[20] J. Ye, "PID tuning method using single-valued neutrosophic cosine measure and genetic algorithm," *Intelligent Automation and Soft Computing*, 2018.

[21] Q. Lu, M. Xiao, B. Tao et al., "Complex dynamic behaviors of a congestion control system under a novel PD1n control law: stability, bifurcation and periodic oscillations," *Chaos, Solitons and Fractals*, vol. 126, 2019.

[22] Y. Ji, "Synchronization analysis for master and slave system under communication time delay using fractional-order PD α control," *International Journal of Dynamics and Control*, vol. 7, 2019.

[23] S. Shi, M. Xiao, L. N. Rong et al., "Stability and bifurcation control of a neuron system under a novel fractional-order PD controller," *Science China Technological Sciences*, vol. 62, 2019.

[24] H. Bang, M.-J. Tahk, and H.-D. Choi, "Large angle attitude control of spacecraft with actuator saturation," *Control Engineering Practice*, vol. 11, no. 9, pp. 989–997, 2003.

[25] M. J. Sidi, *Spacecraft Dynamics and Control*, Cambridge University Press, Cambridge, UK, 2014.

[26] H. Bang, J. Kim, and Y. Jung, "Spacecraft attitude control compensating internal payload motion using disturbance observer technique," *International Journal of Aeronautical and Space Sciences*, vol. 20, 2019.

[27] X. Xu, H. Chen, C. Lian, and D. Li, "Learning-based predictive control for discrete-time nonlinear systems with stochastic disturbances," *IEEE Transactions on Neural Networks and Learning Systems*, vol. 29, 2018.

[28] G. L. O. Serra and C. P. Bottura, "Multiobjective evolution based fuzzy PI controller design for nonlinear systems," *Engineering Applications of Artificial Intelligence*, vol. 19, 2006.

[29] L. E. Ramos-Velasco, O. A. Domínguez-Ramírez, and V. Parra-Vega, "Wavenet fuzzy PID controller for nonlinear MIMO systems: experimental validation on a high-end haptic robotic interface," *Applied Soft Computing*, vol. 40, 2016.

[30] H. Arpaci and O. F. Ozguven, "Design of adaptive fractional-order PID controller to enhance robustness by means of adaptive network fuzzy inference system," *International Journal of Fuzzy Systems*, vol. 19, 2017.

[31] Q. Zhou, W. Wang, H. Liang, M. Basin, and B. Wang, "Observer-based event-triggered Fuzzy adaptive bipartite containment control of multi-agent systems with input quantization," *IEEE Transactions on Fuzzy Systems*, 2019.

[32] C.-C. Tsai, F.-C. Tai, Y.-L. Chang, and C.-T. Tsai, "Adaptive predictive PID control using fuzzy wavelet neural networks for nonlinear discrete-time time-delay systems," *International Journal of Fuzzy Systems*, vol. 19, no. 6, pp. 1718–1730, 2017.

[33] Q. Liu, J. Leng, D. Yan et al., "Digital twin-based designing of the configuration, motion, control, and optimization model of a flow-type smart manufacturing system," *Journal of Manufacturing Systems*, 2020.

[34] Q. Zhou, P. Du, H. Li, R. Lu, and J. Yang, "Adaptive fixed-time control of error-constrained pure-feedback interconnected nonlinear systems," *IEEE Transactions on Systems, Man and Cybernetics: Systems*, 2020.

[35] W. Wang, H. Liang, Y. Pan, and T. Li, "Prescribed performance adaptive fuzzy containment control for nonlinear multi-agent systems using disturbance observer," *IEEE Transactions on Cybernetics*, 2020.

[36] C. C. Tsai, Z. C. Wang, C. T. Lee, and Y. Y. Li, "Intelligent adaptive trajectory tracking control for an autonomous small-scale helicopter using fuzzy basis function networks," *Asian Journal of Control*, vol. 17, 2015.

[37] J. Zhang, Y. Zhang, and C. Xu, "Backing up a truck on Gaussian and non-Gaussian impulsive noise with extended kalman filter and fuzzy controller," *International Journal of Fuzzy Systems*, vol. 20, 2018.

[38] Q. Zhou, W. Wang, H. Ma, and H. Li, "Event-triggered fuzzy adaptive containment control for nonlinear multi-agent systems with unknown Bouc-Wen hysteresis input," *IEEE Transactions on Fuzzy Systems*, 2019.

[39] J. Qiu, K. Sun, T. Wang, and H. Gao, "Observer-based fuzzy adaptive event-triggered control for pure-feedback nonlinear systems with prescribed performance," *IEEE Transactions on Fuzzy Systems*, vol. 27, no. 11, pp. 2152–2162, 2019.

[40] H. Liang, X. Guo, Y. Pan, and T. Huang, "Event-triggered fuzzy bipartite tracking control for network systems based on distributed reduced-order observers," *IEEE Transactions on Fuzzy Systems*, 2019.

[41] P. Wang and D. P. Kwok, "Analysis and synthesis of an intelligent control system based on fuzzy logic and the PID principle," *Intelligent Systems Engineering*, vol. 1, 1992.

[42] H. Boubertakh, M. Tadjine, P.-Y. Glorennec, and S. Labiod, "Tuning fuzzy PD and PI controllers using reinforcement learning," *ISA Transactions*, vol. 49, no. 4, pp. 543–551, 2010.

[43] X. G. Duan, H. X. Li, and H. Deng, "Robustness of fuzzy PID controller due to its inherent saturation," *Journal of Process Control*, vol. 22, 2012.

[44] A. Kumar and V. Kumar, "A novel interval type-2 fractional order fuzzy PID controller: design, performance evaluation, and its optimal time domain tuning," *ISA Transactions*, vol. 68, 2017.

[45] Y. Wang, Q. Jin, and R. Zhang, "Improved fuzzy PID controller design using predictive functional control structure," *ISA Transactions*, vol. 71, 2017.

[46] A. H. Gomaa Haroun and Y. ya Li, "A novel optimized hybrid fuzzy logic intelligent PID controller for an interconnected multi-area power system with physical constraints and boiler dynamics," *ISA Transactions*, vol. 71, 2017.

[47] A. H. Gomaa Haroun and Y.-Y. Li, "Ant lion optimized fractional order fuzzy pre-compensated intelligent pid controller for frequency stabilization of interconnected multi-area power systems," *Applied System Innovation*, vol. 2, 2019.

[48] A. Kosari, H. Jahanshahi, and S. A. Razavi, "An optimal fuzzy PID control approach for docking maneuver of two spacecraft: orientational motion," *Engineering Science and Technology, an International Journal*, vol. 20, 2017.

[49] D. Calvo, T. Avilés, V. Lapuerta, and A. Laverón-Simavilla, "Fuzzy attitude control for a nanosatellite in low Earth orbit," *Expert Systems with Applications*, vol. 58, pp. 102–118, 2016.

[50] Z. Chen, L. Zhong, X. Liu, and B. Cong, "Adaptive fuzzy PD+ control for attitude maneuver of rigid spacecraft," *Asian Journal of Control*, vol. 18, no. 2, pp. 631–641, 2016.

[51] Y.-C. Chak, R. Varatharajoo, and Y. Razoumny, "Disturbance observer-based fuzzy control for flexible spacecraft combined attitude & sun tracking system," *Acta Astronautica*, vol. 133, pp. 302–310, 2017.

[52] N. Najafizadeh, H. Jahanshahi, and M. Fakoor, "Adaptive fuzzy PID control strategy for spacecraft attitude control," *International Journal of Fuzzy Systems*, vol. 21, 2019.

[53] H.-Q. Li, L.-C. Duan, X.-F. Liu, and G.-P. Cai, "Deployment and control of flexible solar array system considering joint friction," *Multibody System Dynamics*, vol. 39, no. 3, pp. 249–265, 2017.

[54] F. Birhanu, Z.-B. Chen, and W. Ma, "Modeling and simulation of satellite solar panel deployment and locking," *Information Technology Journal*, vol. 9, 2010.

[55] E. J. Haug, "Computer aided kinematics and dynamics of mechanical systems. volume 1: basic methods," *Journal of Manufacturing Systems*, vol. 11, 1992.

[56] H. Yamashita, A. I. Valkeapää, P. Jayakumar, and H. Sugiyama, "Continuum mechanics based bilinear shear deformable shell element using absolute nodal coordinate formulation," *Journal of Computational and Nonlinear Dynamics*, vol. 10, 2015.

[57] H. Yamashita, P. Jayakumar, and H. Sugiyama, "Development of shear deformable laminated shell element and its application to ANCF tire model," in *Proceedings of the Volume 6: 11th International Conference on Multibody Systems,*

Nonlinear Dynamics, and Control, Boston, MA, USA, August 2015.

[58] E. N. Dvorkin and K. J. Bathe, "A continuum mechanics based four-node shell element for general non-linear analysis," *Engineering Computations*, vol. 1, no. 1, pp. 77–88, 1984.

[59] P. Betsch and E. Stein, "An assumed strain approach avoiding artificial thickness straining for a non-linear 4-node shell element," *Communications in Numerical Methods in Engineering*, vol. 11, no. 11, pp. 899–909, 1995.

[60] U. Andelfinger and E. Ramm, "EAS-Elements for two-dimensional, three-dimensional, plate and shells and their equivalence to HR-elements," *International Journal for Numerical Methods in Engineering*, vol. 36, pp. 1413–1449, 1993.

[61] J. C. Simo and M. S. Rifai, "A class of mixed assumed strain methods and the method of incompatible modes," *International Journal for Numerical Methods in Engineering*, vol. 29, 1990.

[62] D. García-Vallejo, J. L. Escalona, J. Mayo, and J. Domínguez, "Describing rigid-flexible multibody systems using absolute coordinates," *Nonlinear Dynamics*, vol. 34, no. 1/2, pp. 75–94, 2003.

[63] H. Cheng and K. C. Gupta, "An historical note on finite rotations," *Journal of Applied Mechanics*, vol. 56, 1989.

[64] M. Geradin and D. Rixen, *Mechanical Vibration*, Wiley, Hoboken, NJ, USA, 1997.

[65] D. Negrut, R. Rampalli, G. Ottarsson, and A. Sajdak, "On an implementation of the hilber-hughes-taylor method in the context of index 3 differential-algebraic equations of multibody dynamics (DETC2005-85096)," *Journal of Computational and Nonlinear Dynamics*, vol. 2, no. 1, pp. 73–85, 2006.

[66] B. Hussein, D. Negrut, and A. A. Shabana, "Implicit and explicit integration in the solution of the absolute nodal coordinate differential/algebraic equations," *Nonlinear Dynamics*, vol. 54, no. 4, pp. 283–296, 2008.

[67] Y. Zhang, Q. Tian, L. Chen, and J. Yang, "Simulation of a viscoelastic flexible multibody system using absolute nodal coordinate and fractional derivative methods," *Multibody System Dynamics*, vol. 21, 2009.

[68] C. Yang, Y. Jiang, J. Na, Z. Li, L. Cheng, and C.-Y. Su, "Finite-time convergence adaptive fuzzy control for dual-arm robot with unknown kinematics and dynamics," *IEEE Transactions on Fuzzy Systems*, vol. 27, no. 3, pp. 574–588, 2019.

[69] C. Yang, C. Chen, N. Wang, Z. Ju, J. Fu, and M. Wang, "Biologically inspired motion modeling and neural control for robot learning from demonstrations," *IEEE Transactions on Cognitive and Developmental Systems*, vol. 11, pp. 281–291, 2019.

[70] L. Vu-Quoc and X. G. Tan, "Optimal solid shells for nonlinear analyses of multilayer composites. I. Statics," *Computer Methods in Applied Mechanics and Engineering*, vol. 192, no. 9-10, pp. 975–1016, 2003.